

The Infrared Surface Brightness Fluctuation Hubble Constant¹

Joseph B. Jensen²

Gemini Observatory, 670 N. A'ohoku Pl., Hilo, HI 96720
jjensen@gemini.edu

John L. Tonry

Institute for Astronomy, University of Hawaii
2680 Woodlawn Drive, Honolulu, HI 96822
jt@avidya.ifa.hawaii.edu

Rodger I. Thompson

Steward Observatory, University of Arizona, Tucson, AZ 85721
rthompson@as.arizona.edu

Edward A. Ajhar and Tod R. Lauer

National Optical Astronomical Observatories
P.O. Box 26732, Tucson, AZ 85726
ajhar@noao.edu, lauer@noao.edu

Marcia J. Rieke

Steward Observatory, University of Arizona, Tucson, AZ 85721
mrieke@as.arizona.edu

Marc Postman

Space Telescope Science Institute, 3700 San Martin Dr., Baltimore, MD 21218
postman@stsci.edu

and

Michael C. Liu³

Department of Astronomy, University of California, Berkeley, CA 94720
mliu@triscuit.berkeley.edu

¹Based on observations with the NASA/ESA Hubble Space Telescope, obtained at the Space Telescope Science Institute, which is operated by AURA, Inc., under NASA contract NAS 5-26555.

²Gemini Science Fellow

³Currently Beatrice Watson Parrent Fellow at the University of Hawaii Institute for Astronomy, 2680 Woodlawn Drive, Honolulu, HI 96822, mliu@ifa.hawaii.edu

ABSTRACT

We measured infrared surface brightness fluctuation (SBF) distances to an isotropically-distributed sample of 16 distant galaxies with redshifts reaching $10,000 \text{ km s}^{-1}$ using the near-IR camera and multi-object spectrometer (NICMOS) on the *Hubble Space Telescope* (HST). The excellent spatial resolution, very low background, and brightness of the IR fluctuations yielded the most distant SBF measurements to date. Twelve nearby galaxies were also observed and used to calibrate the F160W ($1.6 \mu\text{m}$) SBF distance scale. Of these, three have Cepheid variable star distances measured with HST and eleven have optical *I*-band SBF distance measurements. A distance modulus of 18.5 mag to the Large Magellanic Cloud was adopted for this calibration. We present the F160W SBF Hubble diagram and find a Hubble constant $H_0 = 76 \pm 1.3$ ($1\text{-}\sigma$ statistical) ± 6 (systematic) $\text{km s}^{-1} \text{Mpc}^{-1}$. This result is insensitive to the velocity model used to correct for local bulk motions. Restricting the fit to the six most distant galaxies yields the smallest value of $H_0 = 72 \pm 2.3 \text{ km s}^{-1} \text{Mpc}^{-1}$ consistent with the data. This 6% decrease in the Hubble constant is consistent with the hypothesis that the Local Group inhabits an under-dense region of the universe, but is also consistent with the best-fit value of $H_0 = 76 \text{ km s}^{-1} \text{Mpc}^{-1}$ at the 1.5-sigma level.

Subject headings: cosmology: distance scale — cosmology: large-scale structure of universe — galaxies: distances and redshifts

1. Introduction

The Hubble constant, H_0 , is the most fundamental of the cosmological parameters. Yet in spite of its key role in our understanding of the universe, an accurate determination of its value eluded researchers for decades. It has only been within the last few years that the promise of knowing H_0 to better than 10% has been realized (Mould et al. 2000). The *Hubble Space Telescope* (HST) has occupied a key role in resolving the debate over the Hubble constant by enabling distance measurements not previously possible from the ground. With HST’s spatial resolution, Cepheid variable stars have been detected in galaxies as distant as 20 Mpc. Cepheid distances to a variety of galaxies, including some in the important Virgo and Fornax clusters, have provided new calibrations of many secondary distance indicators, including type-Ia supernovae (Gibson et al. 2000, Parodi et al. 2000), fundamental plane (Kelson et al. 2000), Tully-Fisher (Sakai et al. 2000), planetary nebulae, globular clusters, and surface brightness fluctuations (Ferrarese et al. 2000a). Uniform HST Cepheid distances were collected by Ferrarese et al. (2000b).

Surface brightness fluctuations have emerged as an accurate and reliable distance indicator (Tonry et al. 1997, Blakeslee et al. 1999). HST has made it possible to not only better calibrate SBFs by providing Cepheid distances to calibration galaxies, but also allowed detection of fluctuations in half a dozen galaxies at much greater distances than possible from the ground (Lauer

et al. 1998, Pahre et al. 1999, Thomson et al. 1997). Two additional low signal-to-noise ratio (S/N) measurements in the Coma cluster (Thomson et al. 1997, Jensen et al. 1999), were the most distant SBF measurements until the current NICMOS project.

Surface brightness fluctuations have a much larger amplitude in the near-IR than at optical wavelengths. The Near Infrared Camera and Multi-object Spectrograph (NICMOS) on the HST provides the combination of low background and high spatial resolution needed to measure IR SBFs beyond 100 Mpc for the first time. The purpose of this study was to calibrate the F160W SBF distance scale and to measure H_0 beyond the effects of local flows. Reaching distances twice as large as previous SBF studies for a sample uniformly distributed on the sky provided immunity to many of the difficulties that plague all attempts to measure H_0 within 50 Mpc.

In the next section we describe the selection of the calibration and distant galaxy samples observed. In Section 3 we discuss the procedures used to acquire and reduce the data. Section 4 describes the methods used to determine the SBF amplitude. Section 5 discusses the empirical calibration of the F160W SBF distance scale and the comparison to stellar population models. Section 6 presents the IR SBF Hubble diagram. Finally, we discuss the relationship of our measurement to others which find lower values of H_0 and conclude with a summary section.

2. Sample Selection

As part of our program to measure distances to redshifts of $10,000 \text{ km s}^{-1}$, we observed a set of nearby galaxies in the Leo, Virgo, and Fornax clusters. These observations support an empirical distance calibration determined both using Cepheid variable star distances and the extensive I -band SBF distance survey (Tonry et al. 1997). The calibration galaxies cover a similar color range as the distant galaxies used to measure H_0 (I -band SBF brightnesses show a systematic dependence on galaxy $(V-I)$ color). In addition to our calibration data, we discovered that several other NICMOS programs included F160W observations of nearby galaxies suitable for SBF analysis that could be used to augment our calibration. The most useful of these are the IR SBF survey of the Fornax cluster (NICMOS program 7458, J. R. Graham et al.) and the programs which targeted galaxies previously observed using WFPC-2 for the purpose of measuring Cepheid distances. We acquired raw NICMOS data from the HST archive and reduced it using the procedures presented in this paper to guarantee a completely consistent calibration.

Because we were able to analyze F160W NICMOS data for galaxies with Cepheid distances, we were not required to assume that the ellipticals and spirals in a given cluster are all at a common distance. For at least a few Cepheid-bearing spirals, IR SBF measurements are possible in their bulges. Using a calibration based solely on galaxies with distances measured both using Cepheid variables and SBFs removes the added uncertainty in the calibration arising from the size and distribution of galaxies in the clusters (Tonry et al. 2000, hereafter SBF-II).

In addition to the relatively local calibrators, we also targeted five galaxies with I -band SBF

Table 1. F160W NICMOS Observations

Galaxy/Cluster		NICMOS Program	Galactic long lat		A_B (mag) ^a	A_H (mag) ^b	Exposure (sec)
<i>Nearby Calibrators</i>							
IC 2006	Fornax	7458	237.51	−50.39	0.048	0.006	256
NGC 1380	Fornax	7458	235.93	−54.06	0.075	0.010	256
NGC 1381	Fornax	7458	236.47	−54.04	0.058	0.008	256
NGC 1387	Fornax	7458	236.82	−53.95	0.055	0.007	256
NGC 1399	Fornax	7453	236.72	−53.63	0.058	0.008	384
NGC 1404	Fornax	7453	236.95	−53.55	0.049	0.006	384
NGC 3031	M 81	7331	142.09	+40.90	0.347	0.046	384
NGC 3351	Leo I	7330	233.95	+56.37	0.120	0.016	640
NGC 3379	Leo I	7453	233.49	+57.63	0.105	0.014	384
NGC 4406	Virgo	7453	279.08	+74.63	0.128	0.017	384
NGC 4472	Virgo	7453	286.92	+70.20	0.096	0.012	384
NGC 4536	Virgo	7331	292.95	+64.73	0.079	0.013	384
NGC 4636	Virgo	7886	297.75	+65.47	0.124	0.016	640
NGC 4725	...	7330	295.08	+88.36	0.051	0.007	320
<i>Intermediate-Distance Galaxies</i>							
NGC 708	Abell 262	7453	136.57	−25.09	0.379	0.050	960
NGC 3311	Abell 1060	7820	269.60	+26.49	0.343	0.046	2560
IC 4296	Abell 3565	7453	313.54	+27.97	0.265	0.035	1920
NGC 7014	Abell 3742	7453	352.53	−42.35	0.142	0.019	1600
NGC 4709	Centaurus	7453	302.66	+21.49	0.512	0.068	1600
NGC 5193	(Abell 3560) ^c	7453	312.59	+28.88	0.242	0.032	1920
<i>Distant Galaxies</i>							
PGC 015524	Abell 496	7453	209.58	−36.49	0.602	0.079	5760
NGC 2832	Abell 779	7453	191.09	+44.39	0.073	0.010	1920
IC 4051	Abell 1656(a)	7820	56.22	+87.72	0.046	0.006	2560
NGC 4874	Abell 1656(b)	7820	58.06	+88.01	0.037	0.005	2560
NGC 6166	Abell 2199	7453	62.93	+43.69	0.050	0.007	4160
NGC 7768	Abell 2666	7453	106.71	−33.81	0.167	0.022	1600
NGC 2235	Abell 3389	7453	274.67	−27.43	0.330	0.044	2048
IC 4374	Abell 3581	7453	323.14	+32.85	0.263	0.035	1280
IC 4931	Abell 3656	7453	1.92	−29.46	0.306	0.040	1920
NGC 4073	...	7820	276.91	+62.37	0.117	0.016	2560

^aSFD extinctions and assuming $A_B = 4.315E(B - V)$

^bUsing $A_H = 0.132A_B$ (SFD)

^cWillmer et al. 1999 concluded that NGC 5193 is a foreground galaxy, and not a member of the much more distant Abell 3560 cluster.

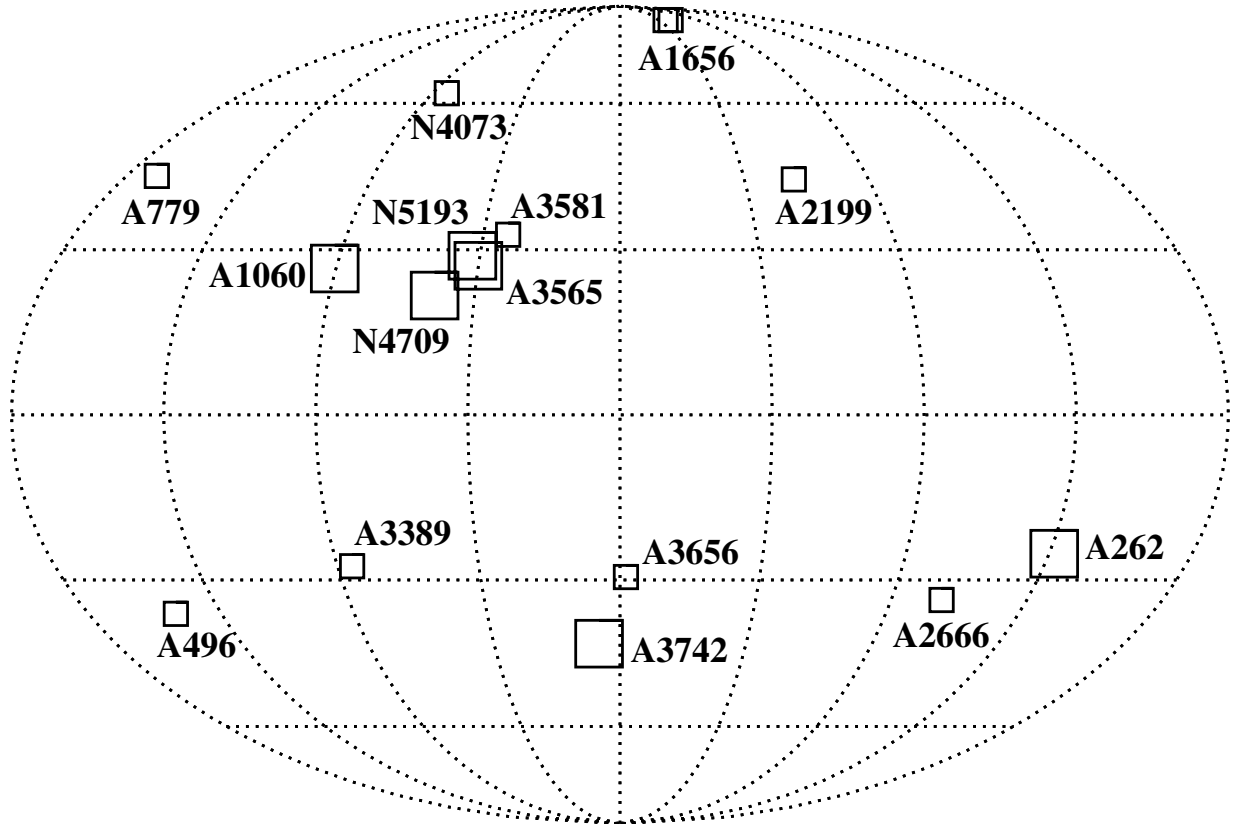


Fig. 1.— Distribution of intermediate-distance (large squares) and distant (small squares) galaxies of our sample, plotted in galactic coordinates. The distant clusters were selected to allow a determination of the Hubble constant that is insensitive to local flows. The intermediate-distance galaxies were chosen to provide overlap with optical I -band SBF measurements.

distances previously measured using WFPC-2: the four from Lauer et al. (1998) and Ajhar et al. (1997), and NGC 4709 in the Centaurus cluster (Optical SBF team, private communication). These intermediate-distance galaxies provide overlap between our local calibration and the distant galaxies from which we determine H_0 . NGC 3311 in the Hydra cluster (NICMOS program 7820, D. Geisler et al.) was added to the intermediate-distance set, although it does not have an I -band SBF distance measurement.

The main focus of this study is to measure distances to the set of 16 galaxies (including the six intermediate-distance galaxies) that extend out to redshifts of $10,000 \text{ km s}^{-1}$. The most distant galaxies are uniformly distributed on the sky to provide a robust determination of H_0 and minimize sensitivity to bulk streaming motions in the local universe. The sample and observational data are presented in Table 1; the positions of the galaxies on the sky are shown in Figure 1 in galactic coordinates.

The results presented in this paper are derived from data taken as part of six separate NICMOS programs. In some cases the observers in these other programs were careful to ensure that their data would be useful for SBF measurements. This program demonstrates the value of the HST archive.

3. Observations and Data Reduction

All the data were acquired using the background-minimizing F160W filter ($1.6 \mu\text{m}$, similar to the standard H filter) and the NIC2 camera read out in the MULTIACCUM mode. NIC2 has a plate scale of 0.075 arcsec per pixel which gives a field of view 19.2 arcsec across. Data were reduced using modified versions of IDL routines developed by the NICMOS team. During each exposure, the NIC2 array was read non-destructively several times, and intermediate images from the MULTIACCUM sequence were created by subtracting the initial read from the intermediate reads. A dark current image from the NICMOS team’s library was then subtracted and pixels exhibiting non-linear response were identified. The differences between intermediate reads were used to identify pixels affected by cosmic rays, which were recognizable as a change in the rate of accumulation of flux in a pixel and could be corrected using the unaffected sub-images. Remaining cosmic rays were fixed when the individual MULTIACCUM images were combined. The next step was to construct the full exposure by multiplying the fitted slope of flux accumulation in each pixel by the total exposure time, divide by the flat field, and mask bad pixels. The combined MULTIACCUM images were then registered to the nearest pixel and added together; integer-pixel registration does not introduce correlations in the noise between pixels that change the spatial power spectrum of the noise. The SBF analysis assumes that the noise is uncorrelated between pixels.

Raw NICMOS images frequently have slightly different bias levels in each quadrant. In the final coadded images, the background level mismatches between quadrants produce horizontal and

vertical discontinuities that affect the measurement of the SBF spatial power spectrum. To remove the offsets, we first processed each individual image and subtracted a smooth fit to the galaxy. The differences between residual background levels in narrow regions on either side of the boundaries were measured. Overall offsets were then computed to effectively add zero flux to the overall image background while minimizing the differences across boundaries. Offsets were applied to the images prior to dividing by the flat field. The final coadded images are much smoother and do not suffer from discontinuities in the background.

Once the relative bias levels between quadrants was removed, the overall bias level remained uncertain. Any such background not removed prior to dividing by the flat field image carries the power spectrum of the flat field into the final spatial power spectrum. The NIC2 flat field has significant structure, making it necessary to address the possibility that residual bias adds power to the measured SBF power spectrum. To measure the influence of residual bias levels on the SBF measurement, we constructed an image composed of scaled copies of that flat field added with the offsets of the dither pattern. The resulting image was then scaled to form a “residual bias image” and added to or subtracted from the final galaxy image prior to SBF analysis. The SBF analysis was repeated for different scale factors, corresponding to the likely range of residual bias values. The most likely residual bias level was determined by trial and error: if a residual bias correction was similar to the level of the inter-quadrant bias adjustment, resulted in lower fluctuation amplitudes, and made the fit to the power spectrum better over a larger range of wavenumber, then it was adopted. If adding a scaled residual bias image led to a worse fit to the spatial power spectrum, or increased the fluctuation amplitude, then no correction was adopted. In many cases applying a residual bias correction did not make the power spectrum fit better or worse, and no correction was adopted. The influence of residual bias on the final SBF measurement was included in the uncertainty by noting the change in the fluctuation magnitude resulting from a range of applied residual bias levels.

Some raw NIC2 images were also affected by interference from the operation of the other cameras. Because NIC1 and NIC3 were not operated in precisely the same mode as NIC2, the cameras were not being reset and read at the same time. Interference between cameras resulted in dark and light horizontal lines in the raw images that adversely affect the SBF power spectrum. To remove the lines, we first identified the affected rows in each individual image with a smooth galaxy profile removed. These rows were masked before the final image was constructed.

A few cosmic rays were energetic enough to leave a residual ghost that persisted for several minutes in the subsequent MULTIACCUM sequences. We identified these occasional residual cosmic rays and masked them as well. These, along with any cosmic rays that escaped detection in the MULTIACCUM sequence, were fixed using valid data for the same location on the sky from the other images in the dither sequence. Each individual exposure (a complete MULTIACCUM sequence) was dithered by 1.5 arcsec, or 20 pixels. When the final summed images were created, we also used the spatial information in the dither sequence to fix the lines caused by read out interference. The final images are smooth and clean, free from almost all the defects inherent in

the raw images.

Even when great care was taken to remove cosmic rays and detector artifacts, one type of persistent problem proved to be difficult to remove from our data. When the HST passed through the South Atlantic Anomaly (SAA), the NICMOS arrays were completely saturated with cosmic rays. The arrays were turned off during these passages. However, some of the time the arrays were restarted too soon after passage through the SAA, and the number of hard cosmic ray hits was very high. The persistent images from these cosmic rays are obvious in the first MULTIACCUM sequences taken after passing through the SAA, and slowly decay through several subsequent exposures.

The background of residual cosmic rays is best described as a “wormy” pattern, with small, sometimes elongated patches of several pixels having significantly higher signal than surrounding regions. An example of this wormy background is shown for one quadrant in subsequent MULTIACCUM images in Figure 2, in which the galaxy profile has been subtracted to show the background. The “worms” make up the splotchy background (left panel) and are distributed fairly uniformly over the array because they correspond to the locations of cosmic ray hits. Worms are a serious concern for SBF measurements, as they are not confined to a small number of pixels. Their spatial power spectrum, while not exactly matching the PSF power spectrum, has significant power on the spatial scales used to fit the SBF power spectrum. If not removed, the power in worms can dominate the stellar fluctuations. The low level persistence of the wormy background pattern can bias the SBF measurement because worms add power to the fluctuation power spectrum, even when they are no longer obvious in the images.

To deal with the worms, we started by examining the galaxy-subtracted residual images from individual MULTIACCUM sequences (e.g., Fig. 2) and we excluded the badly affected images. The remaining question, then, is to what extent the rest of the images were affected. The power spectra from sequential exposures showed the total power decaying to an asymptotic value, although it was difficult to know if the contribution from worms at the asymptotic power level was zero or not. Because the worms were not convolved with the PSF, it was sometimes possible to identify wormy images from power spectra that deviated systematically from the PSF power spectrum. A wormy image has more power at high wavenumbers (small scales) and less power at low wavenumbers than the PSF. To estimate the maximum contribution from residual worminess, we examined the behavior of the SBF signal as a function of the distance from the center of the galaxy. The stellar SBF signal scales with the galaxy surface brightness, while any background fluctuation power from cosmic ray image persistence is uniform. The result of background worminess was a fluctuation power that increased with the area of the region being analyzed. We measured the SBF power in three or four apertures centered on the galaxy nucleus, and, assuming the stellar population of the galaxy is reasonably uniform (ie., the intrinsic stellar fluctuation magnitude does not change drastically with radius), we applied a correction proportional to area to make the fluctuation measurements in the different annuli equal, if possible. The details of these corrections are discussed further in the appendix.

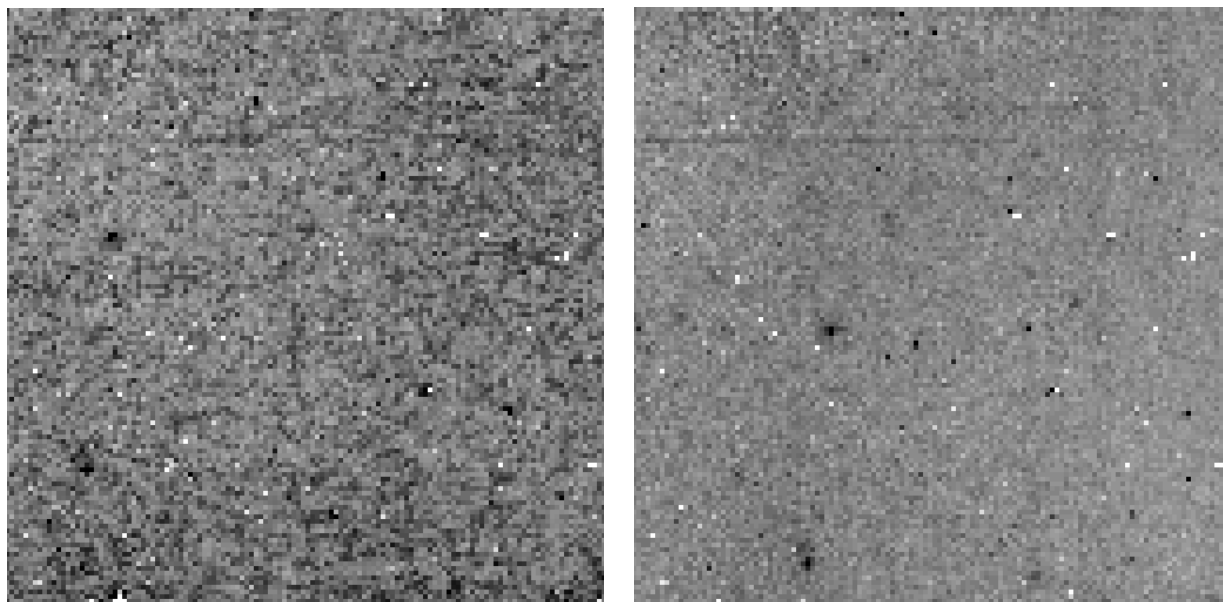


Fig. 2.— The same quadrant (9.6 arcsec across) from two of the individual exposures of Abell 3389 are shown with the galaxy subtracted. The frame on the left shows a very “wormy” background in which many pixels are contaminated. The black speckles not seen in the image on the right are residual images of cosmic rays. The right image was taken 37 minutes later, when the residual background had largely faded. Both images are displayed using the *same* linear grayscale.

4. SBF Measurements

We followed the same basic procedures for measuring SBF amplitudes outlined in detail in Jensen et al. (1998). We first fitted and subtracted a smooth fit to the galaxy profile. Fluctuations can be seen in the three examples shown in Figure 3. Objects in the galaxy-subtracted image were identified, their brightnesses and number densities measured, and a luminosity function generated for globular clusters (GCs) and background galaxies (see Jensen et al. 1998 for details of the luminosity function fits). Objects down to the completeness limit were masked, and the luminosity function integrated beyond the completeness limit to determine the contribution to the SBFs from undetected globular clusters and galaxies. The SBF analysis is insensitive to the exact values assumed for the globular cluster luminosity function width and peak magnitude or the galaxy luminosity function slope when the brightest of these populations are well-measured and masked. Residual large-scale variations in the background resulting from incomplete galaxy subtraction were fitted and removed as well; low wavenumbers ($k < 20$) were ignored in fitting the power spectrum because the spectrum at low wavenumbers was modified by the background subtraction. The fitting parameters for the galaxy profile and large-scale background were tuned to produce the cleanest power spectrum possible. The uncertainties resulting from the galaxy and background fits were determined and added in quadrature with the other sources of uncertainty. Dusty regions near the centers of a few of the galaxies were masked.

The SBF spatial power spectrum normalized by the mean galaxy surface brightness was fitted with the sum of a white-noise component P_1 and the expectation power spectrum $E(k)$ scaled by the fluctuation power P_0 . $E(k)$ is a combination of the normalized PSF power spectrum and the mask used to excise point sources and select the radial region of the galaxy being analyzed. The data were fitted with the function

$$P(k) = P_0 E(k) + P_1. \quad (1)$$

The fluctuation power P_0 must be corrected for undetected point sources and residual wormy background. These are represented by P_r and P_g , respectively. The power in stellar SBFs is therefore

$$P_{\text{fluc}} = P_0 - P_r - P_g. \quad (2)$$

P_{fluc} is simply a flux, and has units of electrons per pixel per integration time. Fluctuation powers and the relative sizes of the P_r and P_g corrections are listed in Table 2. P_{fluc} can be transformed into an apparent fluctuation magnitude and corrected for galactic extinction:

$$\bar{m} = -2.5 \log(P_{\text{fluc}}) + m_1 - A_H \quad (3)$$

where m_1 is the magnitude of a source yielding 1 e^- per total integration time on the Vega system. We adopted the photometric zero point for NIC2 and the F160W filter measured by the NICMOS team of $m_1 = 23.566 \pm 0.02$ mag, the brightness of a source which gives 1 $e^- s^{-1}$. The gain is 5.4 e^- per ADU. In this paper we have chosen to adopt the extinction values of Schlegel et al. (1998,

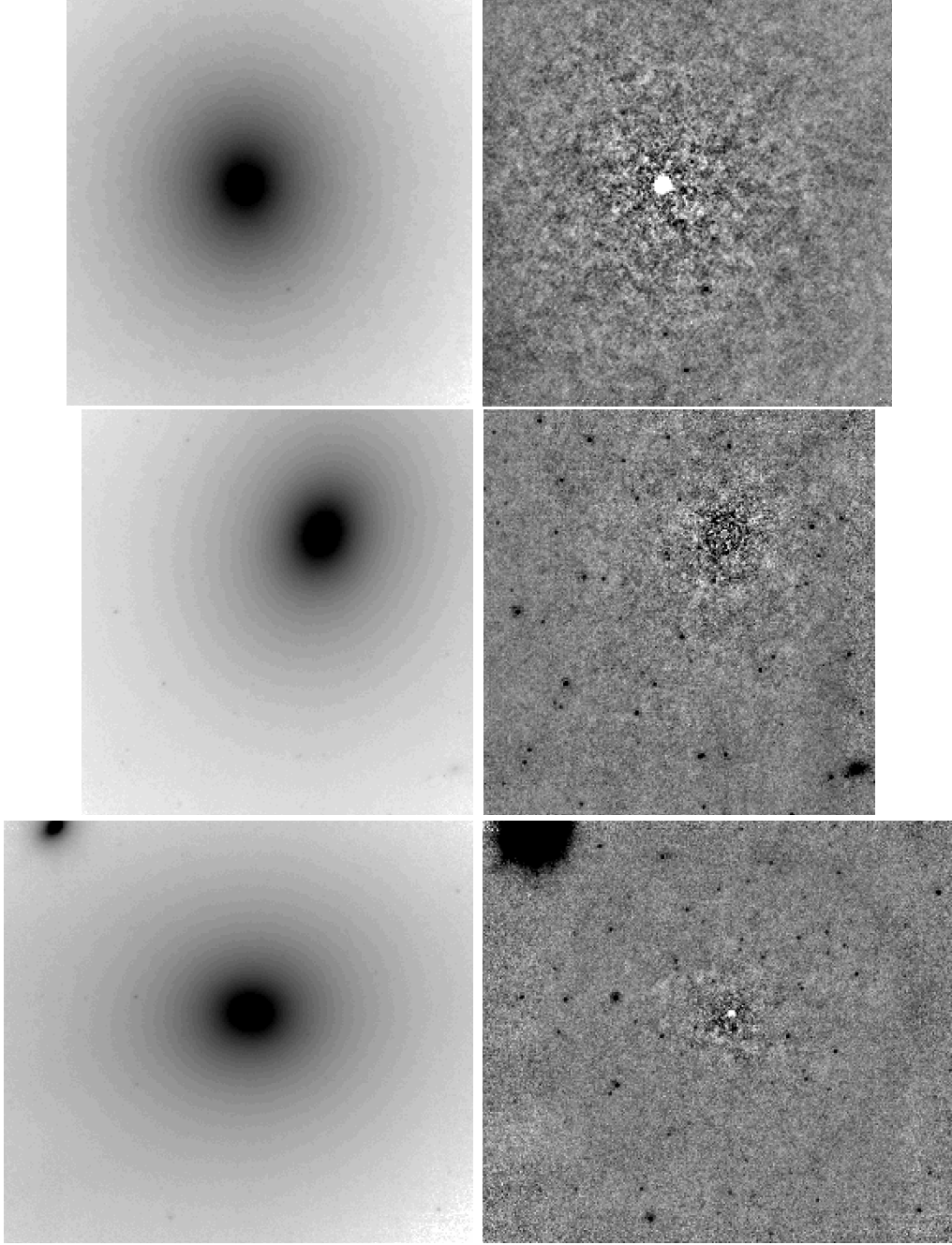


Fig. 3.— Representative images for NGC 3379 (top), NGC 4709 (middle), and Abell 496 (bottom). The images on the left are printed with a square-root stretch, and the galaxy-subtracted images on the right are shown using a simple linear gray scale. Point sources in the galaxy-subtracted images are masked prior to measuring the surface brightness fluctuations. The fluctuations are easily visible as bumpiness in the background seen in all of the field of view of NGC 3379 and near the center of Abell 496. The globular cluster populations can also be seen in the images of NGC 4709 and Abell 496. The images differ slightly in size because of the dither pattern used, but all are approximately 20 arcmin across. The position angle on the sky is different for each galaxy.

hereafter SFD), which are converted to the H -band extinction values assuming $A_B = 4.315 E(B-V)$ and $A_H = 0.132 A_B$ (SFD).

Because the stellar SBF pattern is convolved with the diffraction pattern of the telescope and instrument, we require a good measurement of the point spread function (PSF) for each observation. If the reference PSF shape used does not match the PSF of the data, the fit will be poor. If the PSF is not properly normalized, the photometry will not be correct. To ensure a good SBF measurement, we attempted to image a bright star concurrently with each galaxy observation to serve as a high-S/N PSF reference. The PSF star measurements were short, unguided exposures, and in some cases the PSF was blurred slightly by telescope drift. Others were unusable because of close companions that were undetectable without the excellent resolution of the HST. Still another turned out to be a compact galaxy. In the end, we acquired 10 good PSF measurements over the course of our program (spanning approximately 1 year). For each SBF measurement, we chose the PSF taken closest in time to the galaxy observation.

The uncertainty in the SBF measurement resulting from variations in the PSF was determined by using all 10 PSF stars to measure the fluctuation magnitude for a galaxy. The standard deviation in each case was added in quadrature with the other sources of uncertainty, and was typically between 4% and 6%. The time between individual PSF measurements was much longer than the “breathing” timescale of the telescope, so the variation between PSFs was random. In general, the PSF fits to the SBF data were excellent. While the PSF shows diffraction rings and spots that are quite different from the typical smooth PSF observed from the ground, the PSF power spectrum fits the galaxy data very well, both in the tight Airy core (the broad, high-wavenumber component) and in the wings (the steeper component at low wavenumbers).

We compared our snapshot PSF measurements to 16 measurements of four stars made by the NICMOS team. Fluctuation measurements of our most distant galaxy (Abell 496) were made using the library PSFs as a test case. The library PSF results agreed perfectly with measurements made using our snapshot PSFs, and showed a somewhat smaller scatter (3.5%). The smaller dispersion can be attributed to the fact that the library PSF measurements were made on fewer stars and while the telescope guiding was enabled.

The signal-to-noise ratio of an SBF measurement is best quantified as

$$\xi = P_{\text{fluc}} / (P_1 + P_g). \quad (4)$$

Jensen et al. (1998) showed that ξ is a good figure of merit for IR SBF measurements. Values of ξ less than unity indicate measurements that are unreliable. The higher ξ , the better the SBF measurement. Galaxies with $\xi < 1$ are necessarily those for which the correction for globular clusters (P_r) or residual cosmic rays (P_g) are large. P_0/P_1 , while sometimes used as a measure of SBF S/N, significantly overestimates the true S/N because P_0 contains the contributions from these other sources of variance.

In several cases, the relative contributions of stellar SBFs (P_{fluc}), background worminess (P_g),

Table 2. Distant F160W SBF Measurements

Galaxy/ Cluster	Annulus (arcsec)	P_0 ($e^- \text{pix}^{-1}$)	P_1/P_0	P_r/P_0	P_g/P_0	ξ	P_{fluc} ($e^- \text{pix}^{-1}$)	Notes
Abell 262	2.4–4.8	8.8±0.3	0.22	0.00	0.34	1.2	5.8	d,w
Abell 496	2.4–4.8	11.4±0.8	0.17	0.29	0.11	2.2	6.8	
Abell 779	2.4–4.8	7.3±0.6	0.20	0.28	0.08	2.2	4.6	p
Abell 1060	2.4–4.8	20.7±0.5	0.08	0.09	0.00	12.1	18.7	(d)
Abell 1656(a)	2.4–4.8	15.7±0.6	0.15	0.41	0.16	1.4	6.8	GC
Abell 1656(b)	4.8–9.6	11.7±0.8	0.21	0.15	0.22	1.5	7.4	
Abell 2199	2.4–4.8	9.0±0.3	0.22	0.35	0.00	2.9	5.9	(d)
Abell 2666	2.4–4.8	5.5±0.3	0.33	0.00	0.53	0.6	2.6	w
Abell 3389	2.4–4.8	8.2±0.2	0.24	0.33	0.26	0.8	3.3	w
Abell 3565	4.8–9.6	17.3±1.0	0.12	0.06	0.07	4.7	15.1	(d)
Abell 3581	2.4–4.8	8.4±0.9	0.26	0.18	0.42	0.6	3.4	(d),w
Abell 3656	2.4–4.8	8.0±0.6	0.24	0.10	0.10	2.4	7.0	p
Abell 3742	4.8–9.6	12.1±1.4	0.22	0.10	0.05	3.1	10.3	drift
NGC 4073	2.4–4.8	13.1±0.9	0.15	0.31	0.25	1.1	5.8	w
NGC 4709	2.4–4.8	20.2±0.8	0.10	0.08	0.12	3.8	16.3	w
NGC 5193	2.4–4.8	21.4±2.2	0.09	0.07	0.00	10.8	19.9	(d)

Note. — d=extensive dust, (d)=nuclear dust, w=worms, p=dither pattern noise. IC 4051 (Abell 1656a) has an extensive globular cluster population (Baum et al. 1997); Abell 3742 was affected by telescope drift due to failure to lock onto the guide stars.

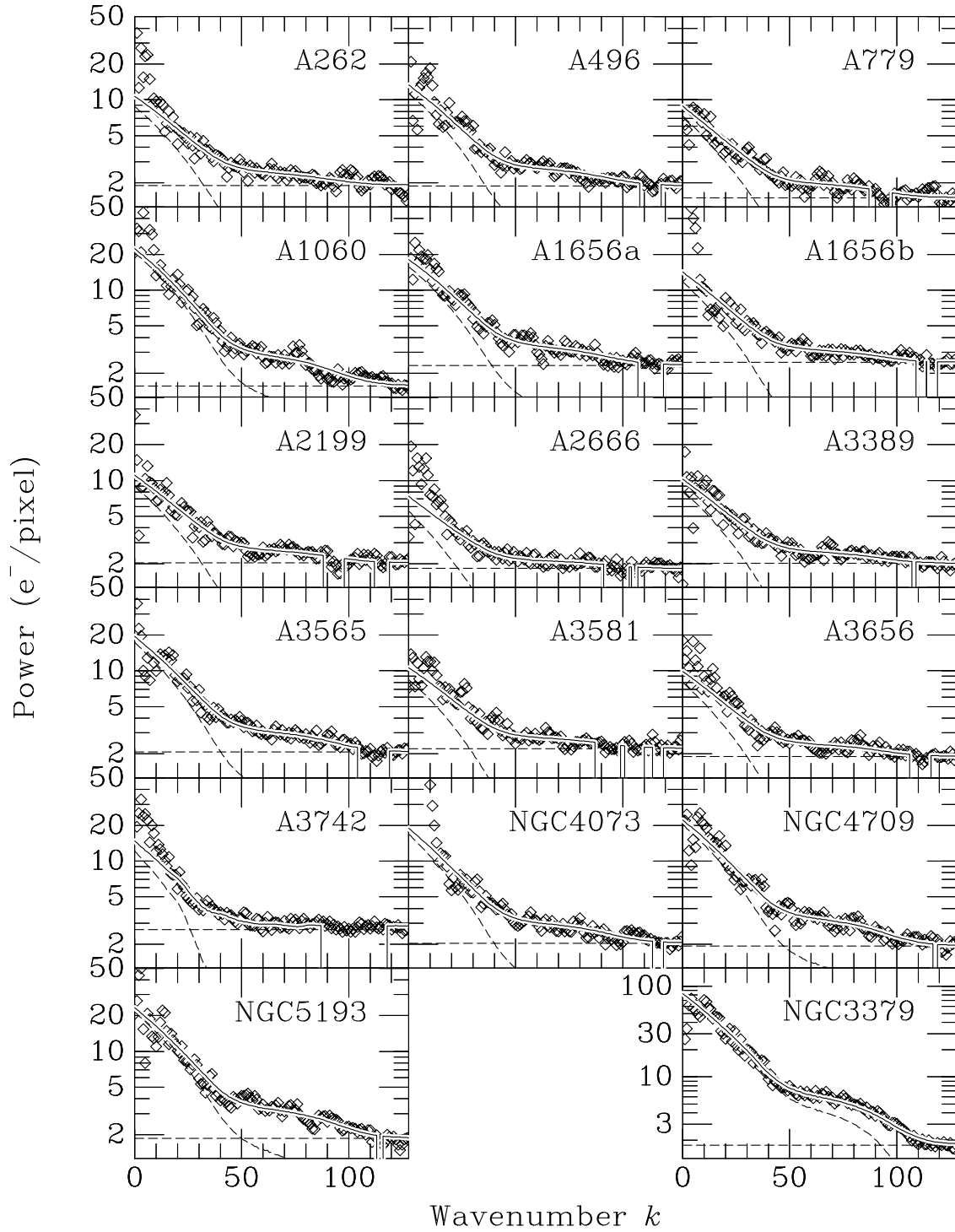


Fig. 4.— Fluctuation spatial power spectra for NGC 3379 and all of the intermediate and distant galaxies. The dashed lines indicate the white-noise component P_1 and the expectation power spectrum (very nearly the power spectrum of the normalized PSF) multiplied by the fluctuation power P_0 . The best fit sum is shown as a solid line. The power spectra shown correspond to the annular regions listed in Table 2.

and globular clusters (P_r) to the power spectrum were difficult to untangle. Table 2 lists the powers measured (in electrons per total integration time) for each galaxy and the relative levels of the P_1 , P_r , and P_g contributions. The fluctuation S/N ratio (ξ) is listed for each galaxy, and the power spectrum for each annulus listed in Table 2 is plotted in Figure 4. Fluctuation measurements were made in three annuli for each galaxy, and the results compared. The inner annulus spanned a radial region from 1.2 to 2.4 arcsec, the middle annulus from 2.4 to 4.8 arcsec, and the outer annulus from 4.8 to 9.6 arcsec. In the appendix we discuss the SBF measurements for each intermediate and distant galaxy individually.

5. Calibration of the F160W SBF Distance Scale

5.1. Absolute Fluctuation Magnitudes

Apparent fluctuation magnitudes for the nearby calibrator galaxies were combined with previously measured distance moduli to empirically determine the absolute brightness of F160W fluctuations \overline{M}_{F160W} . Most of the calibration galaxies are giant ellipticals, and we adopt the distances from the *I*-band SBF survey for them (Optical SBF team, private communication). The *I*-band SBF distances were calibrated using Cepheid distances to a handful of spiral galaxies for which *I*-band SBF analysis was possible in the bulges (SBF-II). Thus the *I*-band SBF distances used to calibrate the F160W distance scale are based on SBF and Cepheid distances to individual galaxies, and do not assume common distances for different galaxies within a cluster or group. Optical SBF distance moduli and F160W fluctuation magnitudes are listed in Table 3.

Four Cepheid-bearing galaxies were observed as part of other NICMOS programs, which allowed us to bypass the *I*-band SBF calibration altogether. We determined reliable \overline{M}_{F160W} values for three of the galaxies using HST Cepheid distances; the fluctuation measurement in NGC 4536 was contaminated by clumpy dust, and it was excluded from the calibration. Cepheid distances are also compiled in Table 3.

The measured apparent fluctuation magnitudes are very robust. Because slewing between targets and acquiring guide stars takes a significant fraction of an HST orbit, only one or two calibration galaxies could be observed in one orbit. Each integration was at least 256 s, far longer than the minimum time needed to measure SBFs with NICMOS at distances less than 20 Mpc. As a result, the fluctuations were very strong in the calibration images, and the corrections for undetected globular clusters and worms were insignificant. The S/N ratios of the calibration measurements were $\xi=15$ to 50.

Absolute fluctuation magnitudes are plotted as a function of $(V-I)$ color in Figure 5. NGC 1387 and NGC 4536 are excessively dusty, and the extra spatial power from the clumpy dust leads to the anomalously bright fluctuation magnitudes measured (they lie outside the range plotted in Figure 5). The dust is easily seen in the NICMOS images, and these two galaxies were rejected

Table 3. F160W SBF Calibration Measurements

Galaxy/ Cluster	$\overline{m}_{\text{F160W}}$ (mag)	$(V-I)_0$ (mag)	<i>I</i> -band SBF Distances		Cepheid Distances	
			$(m-M)_{\overline{I}}$ (mag)	$\overline{M}_{\text{F160W}}$ (mag)	$(m-M)_{\text{Ceph}}^{\text{a}}$ (mag)	$\overline{M}_{\text{F160W}}$ (mag)
<i>Nearby Calibrators</i>						
IC 2006	26.58 ± 0.05	1.183 ± 0.018	31.59 ± 0.29	-5.01 ± 0.29
NGC 1380	26.40 ± 0.05	1.197 ± 0.019	31.32 ± 0.18	-4.92 ± 0.18
NGC 1381	26.52 ± 0.10	1.189 ± 0.018	31.28 ± 0.21	-4.76 ± 0.23
NGC 1387 ^b	26.0 ± 0.7	1.208 ± 0.047	31.54 ± 0.26	-5.6 ± 0.8
NGC 1399	26.76 ± 0.04	1.227 ± 0.016	31.50 ± 0.16	-4.74 ± 0.15
NGC 1404	26.66 ± 0.08	1.224 ± 0.016	31.61 ± 0.19	-4.95 ± 0.19
NGC 3031	22.96 ± 0.05	1.187 ± 0.011	27.96 ± 0.26	-5.00 ± 0.26	27.80 ± 0.08	-4.84 ± 0.09
NGC 3351 ^c	25.16 ± 0.07	1.225 ± 0.014	30.01 ± 0.08	-4.85 ± 0.10
NGC 3379	25.23 ± 0.08	1.193 ± 0.015	30.12 ± 0.11	-4.89 ± 0.13
NGC 4406	26.23 ± 0.06	1.167 ± 0.008	31.17 ± 0.14	-4.94 ± 0.14
NGC 4472	26.23 ± 0.04	1.218 ± 0.011	31.06 ± 0.10	-4.83 ± 0.09
NGC 4536 ^{b,c}	25.43 ± 0.12	1.20 ± 0.07	30.95 ± 0.07	-5.52 ± 0.14
NGC 4636	26.07 ± 0.08	1.233 ± 0.012	30.83 ± 0.13	-4.76 ± 0.15
NGC 4725	25.69 ± 0.10	1.209 ± 0.023	30.61 ± 0.34	-4.92 ± 0.35	30.57 ± 0.08	-4.88 ± 0.12
<i>Intermediate-Distance Galaxies</i> ^d						
Abell 262 ^b	29.06	1.275 ± 0.015	33.99 ± 0.20	-4.96
Abell 3565	28.79	1.199 ± 0.015	33.69 ± 0.16	-4.92
Abell 3742	29.03	1.248 ± 0.015	34.00 ± 0.15	-5.00
NGC 4709	28.48	1.221 ± 0.015	33.04 ± 0.17	-4.58
NGC 5193	28.49	1.208 ± 0.015	33.51 ± 0.15	-5.04

^aFerrarese et al. 2000a

^bSignificant dust; exluded from $\overline{M}_{\text{F160W}}$ calibration.

^c $(V-I)$ color measured in a region matching the NICMOS field of view; the others were measured in larger apertures.

^dF160W SBF magnitudes, distances, and uncertainties for the intermediate set are listed in Table 4. *I*-band SBF distance moduli from Lauer et al. 1998 have been recalculated using SFD extinction corrections. Absolute F160W fluctuation magnitudes are listed here for comparison to the calibration sample.

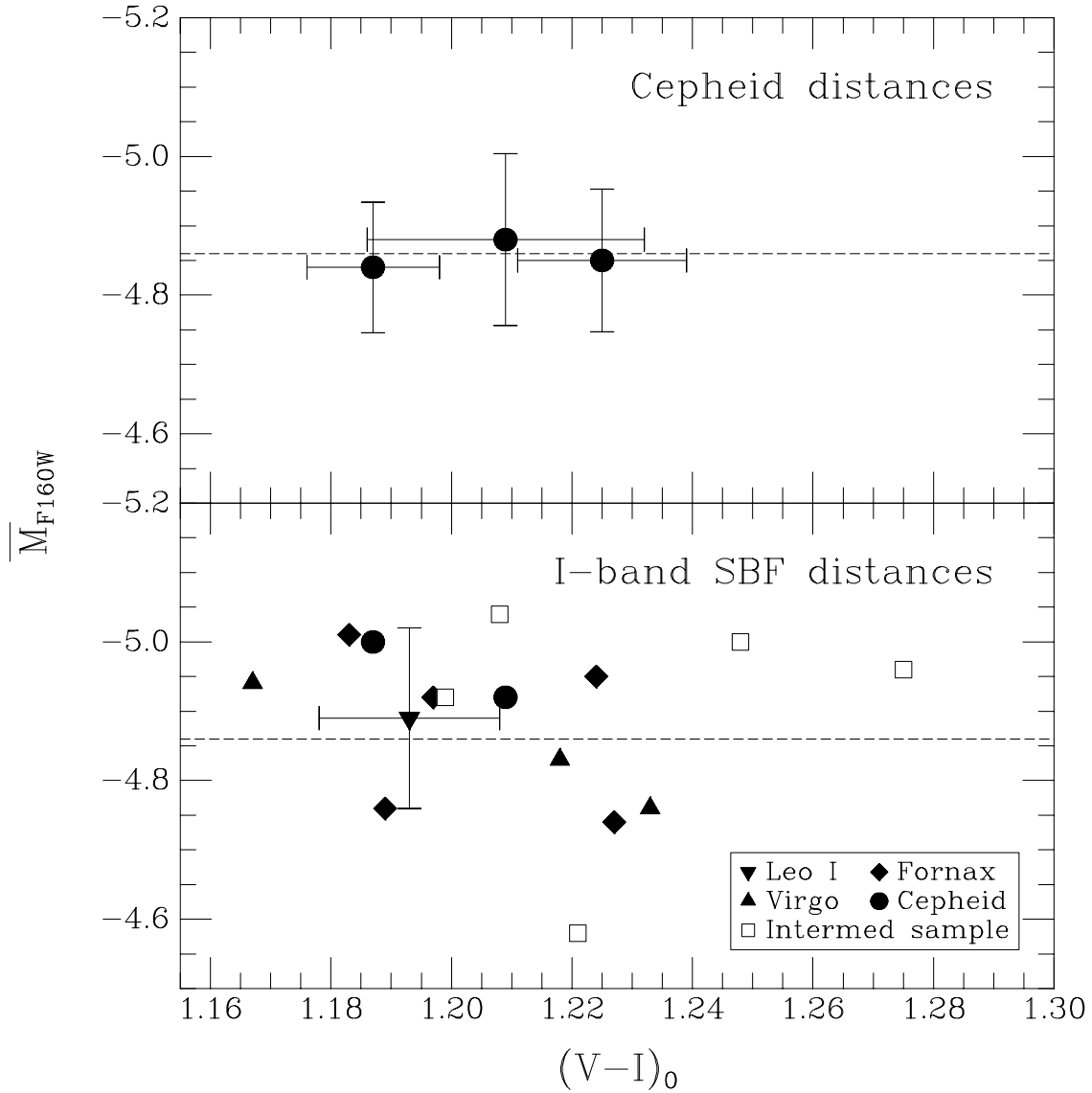


Fig. 5.— Absolute fluctuation magnitudes \overline{M}_{F160W} as a function of galaxy color $(V-I)_0$, corrected for extinction. The upper panel shows the three galaxies for which we have reliable F160W fluctuation magnitudes and Cepheid distances. In the lower panel we plot \overline{M}_{F160W} for the calibrators using their I -band SBF distances. Error bars are shown for NGC 3379, and are typical for the set of calibrators. Note that two of the galaxies with Cepheid distances also have I -band SBF measurements. The horizontal line indicates the calibration $\overline{M}_{F160W} = -4.86 \pm 0.05$ adopted here. The open symbols in the lower panel are the intermediate-distance galaxies with I -band SBF distances measured using WFPC-2 and have similar uncertainties. They were not used in generating the calibration fit (including them only changes the fitted \overline{M}_{F160W} by 0.015 mag). They are shown here to demonstrate that the calibration derived using relatively nearby spirals and ellipticals applies equally well to the brightest cluster galaxies of our distant set.

from further consideration based on morphology, not their bright fluctuation magnitudes. They were excluded from the calibration fits. The top panel of Figure 5 shows $\overline{M}_{\text{F160W}}$ derived using Cepheid distances, and the lower panel shows those calculated using I -band SBF distances.

The best fits for the larger I -band SBF calibration and the direct Cepheid calibration are practically identical. A weighted fit (including the uncertainties both in $\overline{M}_{\text{F160W}}$ and $(V-I)$) has no significant slope in $\overline{M}_{\text{F160W}}$ for galaxies redder than $(V-I) > 1.16$. We therefore adopt a uniform $\overline{M}_{\text{F160W}}$ calibration for galaxies in this color range, and note that none of the distant galaxies are likely to have colors bluer than $(V-I) = 1.16$ (as described in the next section). The I -band SBF distances give

$$\overline{M}_{\text{F160W}} = -4.86 \pm 0.05 \text{ mag} \quad (5)$$

with an rms scatter of 0.08 mag. The calibration derived using only the three Cepheid measurements is indistinguishable (-4.85 ± 0.06 mag). The small scatter in values of $\overline{M}_{\text{F160W}}$ for this color range is remarkable, and emphasizes the potential IR SBFs have as a precision distance indicator and probe of stellar populations.

Five additional galaxies from the intermediate-distance sample are plotted in Figure 5 with open symbols. These galaxies have I -band SBF distances measured using HST. They were not included in the calibration fit; instead, their F160W SBF distances were derived using the calibration and they were included in the computation of H_0 . If they had been used as calibrators, the calibration would have been 0.015 mag brighter, which is entirely consistent given the standard deviation of 0.05 mag observed in the $\overline{M}_{\text{F160W}}$ fit. The intermediate set is presented in Figure 5 to demonstrate the overlap between our calibration sample and the distant galaxies from which H_0 is derived. While both intermediate-distance galaxies redder than $(V-I)_0 = 1.24$ have brighter than average absolute fluctuation magnitudes, we cannot assume that redder galaxies have intrinsically brighter fluctuations. In fact, the results of Jensen et al. (2000) suggest that $\overline{M}_{\text{F160W}}$ gets fainter with increasing $(V-I)$. Different stellar population models (Sec. 5.3) provide contradictory predictions for fluctuation magnitudes in galaxies redder than $(V-I) = 1.24$. At this point, we take the conservative approach and adopt a uniform calibration for all the distant galaxies, relying on the overlap (albeit with significant scatter) between the calibrators and the intermediate set. The consistency of $\overline{M}_{\text{F160W}}$ values shown in Figure 5 suggests that there are probably no significant stellar population differences between the distant brightest cluster galaxies, the nearby ellipticals, and the bulges of the Cepheid-bearing spirals that produce large variations in the F160W absolute fluctuation magnitudes.

The two versions of the calibration presented here are not independent; both rely on many of the same Cepheid calibrators and are subject to the same systematic uncertainties of the Cepheid distance scale. These significant uncertainties are very much the topic of current debate, and include the issues of the distance to the Large Magellanic Cloud (Mould et al. 2000), metallicity corrections to the Cepheid distance scale (Kennicutt et al. 1998; Ferrarese et al. 2000a), and blending of images in the most distant Cepheid measurements (Ferrarese et al. 1998, 2000c; Gibson, Maloney, & Sakai 2000; Stanek & Udalski 2000; Mochejska et al. 2000). This study adopts a distance modulus to the

LMC of 18.50 mag. The Cepheid distances adopted are those of Ferrarese et al. (2000b), without the metallicity correction described in Kennicutt et al. (2000).

5.2. $(V-I)$ Colors

As in the optical I -band, $\overline{M}_{\text{F160W}}$ shows a dependence on $(V-I)$ color such that bluer ellipticals have intrinsically brighter fluctuations. Stellar population models predict a breaking of the age and metallicity degeneracy in the near-IR, and the observed slope of $\overline{M}_{\text{F160W}}$ with $(V-I)$ reveals differences between old, metal-poor populations and young, metal-rich galaxies. A sample of NICMOS SBF measurements in galaxies spanning a wide range in $(V-I)$ is presented in a companion paper (Jensen et al. 2000) in which stellar population issues are explored. The slope in $\overline{M}_{\text{F160W}}$ with color among the redder ellipticals $(V-I) > 1.16$ is insignificant (Fig. 5). $(V-I)$ colors have been measured for 7 of the 16 distant galaxies in our sample (Lauer et al. 1998), and all are significantly redder than $(V-I) = 1.16$. Estimates of the $(V-I)$ colors for the rest of the distant sample were made by finding the best-fitting relationship between $(V-I)$ and $(B-R)$ for the 7 galaxies for which both colors are known, and then applying the relationship to the $(B-R)$ data taken from Lauer & Postman (1995). All of the estimated $(V-I)$ colors are significantly redder than 1.16 as well. The mean estimated $(V-I)$ is 1.246 mag with a standard deviation of 0.027 (averaging all 14 galaxies with known $(B-R)$ colors); the mean for the 7 galaxies with measured $(V-I)$ colors is 1.255 mag. Measured or estimated $(V-I)_0$ colors listed in Table 4 have been corrected for extinction and redshift. We therefore feel secure adopting the calibration determined for galaxies redder than 1.16 for the distant sample. Distances to bluer galaxies will require a reliable $(V-I)_0$ color measurement and the full color- $\overline{M}_{\text{F160W}}$ relation to be presented in Jensen et al. (2000).

5.3. Comparison with Single-Burst Stellar Population Models

If the intrinsic luminosity of the brightest stars in a population is known, fluctuation distances can be determined directly without an empirical calibration based on another distance indicator. Stellar population models can be used to compute theoretical absolute fluctuation magnitudes by determining the second moment of the luminosity function for an ensemble of stars of a particular age and metallicity. In practice, we adopt the empirical calibration because of the uncertainties involved in modeling populations and because of the variations in the ages and metallicities of real galaxies. Nevertheless, it is useful to compare the empirical calibration to the theoretical predictions of stellar population models.

In Figure 6 we plotted the same calibration data points shown in Figure 5 over three different sets of models. The top panel shows the recent model predictions of Liu, Charlot, & Graham (2000) for the F160W filter. These are the same models used to compute the redshift corrections $k(z)$ to our fluctuation magnitudes. The models plotted in the middle panel were taken from Blakeslee,

Table 4. F160W SBF Distances and Velocities

Galaxy/ Cluster	\overline{m}_{F160W} (mag)	max (mag)	min (mag)	$(V-I)_0^a$ (mag)	$k(z)^b$ (mag)	$(m-M)^c$ (mag)	d (Mpc)	v_{CMB}^d (km s ⁻¹)	N^e
A262	29.06±0.08	+0.06	-0.36	1.275±0.015	0.027	33.89±0.10	60	4618	128
A496	30.80±0.09	+0.13	-0.18	(1.21)	0.052	35.61±0.11	132	9799	147
A779	30.10±0.09	+0.00	-0.14	(1.28)	0.036	34.92±0.11	97	7089	59
A1060	28.86±0.07	+0.26	-0.01	(1.28)	0.020	33.70±0.08	55	4061	102
A1656(a)	30.00±0.12	+0.16	-0.34	1.297±0.037	0.039	34.82±0.13	92	7245	377
A1656(b)	29.91±0.08	+0.00	-0.32	1.295±0.037	0.039	34.73±0.10	88	7244	377
A2199	30.68±0.11	+0.00	-0.64	...	0.049	35.49±0.12	125	8935	121
A2666	30.50±0.12	+0.69	-0.20	(1.25)	0.044	35.32±0.13	116	7888	30
A3389	30.49±0.10	+1.14	-0.54	(1.24)	0.042	35.31±0.12	115	8105	39
A3565	28.79±0.08	+0.07	-0.02	1.199±0.015	0.019	33.63±0.09	53	4142	15
A3581	29.97±0.08	+0.24	-0.77	(1.27)	0.035	34.80±0.09	91	6778	29
A3656	29.62±0.07	+0.13	-0.07	(1.24)	0.031	34.45±0.09	78	5607	18
A3742	29.03±0.11	+0.05	-0.16	1.248±0.015	0.026	33.86±0.12	59	4801	20
N4073	30.16±0.12	+0.36	-0.67	...	0.032	34.99±0.13	99	6306	1
N4709	28.48±0.07	+0.00	-0.14	1.221±0.015	0.017	33.32±0.08	46	4905	1
N5193	28.49±0.06	+0.36	-0.15	1.208±0.015	0.019	33.33±0.08	46	3920	1

^a $(V-I)_0$ colors were derived from WFPC-2 data (this study and Lauer et al. 1998) and have had SFD extinction and redshift k -corrections applied. Values listed in parentheses are estimates derived from ground-based photometry (Postman & Lauer 1995) in much larger apertures (see text).

^bLiu et al. 2000 model values

^cUncertainties include only the Gaussian uncertainties combined in quadrature with the calibration uncertainty.

^dHeliocentric velocities from Postman & Lauer 1995 (with additional measurements included) were transformed into the cosmic microwave background frame as described in Lineweaver et al. 1996.

^eNumber of galaxies used to determine the cluster velocity.

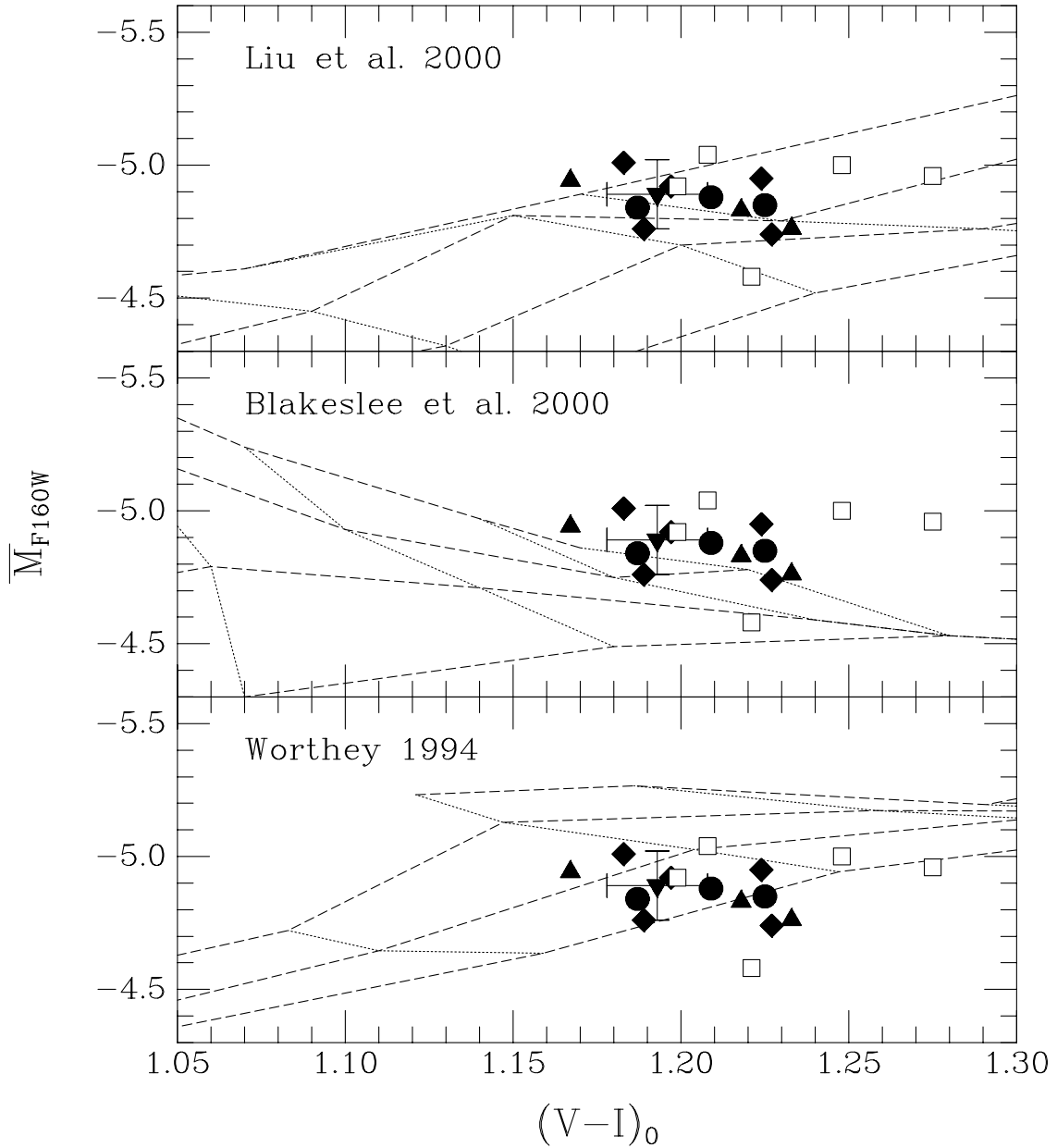


Fig. 6.— The same data shown in Figure 5 plotted over three different sets of stellar population models, as described in the text. The distances used are I -band SBF distances except for the three galaxies with Cepheid distances. The symbol definition is the same as in Figure 5. The bottom dashed lines are 17 Gyr isochrones, followed upward by the 12, 8, and 5 Gyr (top) models (sloping up and to the right in the Liu et al. and Worthey models). The data points are clustered around the solar metallicity tracks in the Liu et al. models, and the next dotted line down and to the left is the $[Fe/H] = -0.4$ set of models. In the middle panel, the points are closest to the $[Fe/H] = 0.2$ models, and extend down to the solar metallicity line. The data points lie closest to the Worthey models with metallicity $[Fe/H] = -0.25$; the lower left line indicates the $[Fe/H] = -0.5$ models.

Vazdekis, & Ajhar (2000). These models were computed for the H -band filter and shifted to F160W using the relation:

$$\overline{M}_{\text{F160W}} = \overline{M}_H + 0.1(\overline{M}_J - \overline{M}_K) \quad (6)$$

(J. Blakeslee, private communication, and Stephens et al. 2000). Finally, Worthey’s (1994) models are plotted in the bottom panel for the F160W filter (G. Worthey, private communication). In all three sets of models, dashed lines indicate isochrones ranging from approximately 5 Gyr at the top to 17 Gyr on the bottom. The fine dotted lines indicate models of constant metallicity. In the Liu et al. case, the SBF measurements straddle the solar-metallicity line, and the next line to the left is $[\text{Fe}/\text{H}] = -0.4$. In the center panel, the points are closest to the $[\text{Fe}/\text{H}] = 0.2$ models of Blakeslee et al. (2000) and reach down to the solar metallicity line. The transformation to the F160W scale, and hence the vertical position of the models, is somewhat uncertain however. In the bottom panel, the points are closest to the $[\text{Fe}/\text{H}] = -0.25$ line; the next metallicity line down is $[\text{Fe}/\text{H}] = -0.5$. The calibration data presented here cover a limited range in color, and appear consistent with stellar populations near solar metallicity (between -0.25 and 0.25) and potentially covering a wide range of ages. A detailed comparison of the models with a NICMOS data set covering a much wider range of $(V-I)$ colors will be presented in Jensen et al. (2000).

6. The F160W SBF Hubble Diagram

6.1. Distances and Uncertainties

To determine the distance to each galaxy, we adopted $\overline{M}_{\text{F160W}} = -4.86 \pm 0.05$ and computed the $k(z)$ -corrected distance modulus:

$$(m-M) = \overline{m}_{\text{F160W}} - \overline{M}_{\text{F160W}} - k(z). \quad (7)$$

Redshift corrections $k(z)$ to fluctuation magnitudes in the F160W-band were taken from the Liu et al. (2000) models for metallicities between $[\text{Fe}/\text{H}] = -0.4$ to 0.0 and old stellar populations. $k(z)$ corrections are listed in Table 4. We compared these $k(z)$ corrections to those determined using Worthey’s models for solar metallicity (G. Worthey, private communication) and found small differences of order $\lesssim 0.01$ mag. At distances of $10,000 \text{ km s}^{-1}$ and less, the magnitude of the $k(z)$ corrections are insensitive to the details of the stellar population models.

The uncertainties in the fluctuation magnitudes in Table 4 are the contributions from PSF fitting, sky subtraction, bias removal, and galaxy subtraction, all added in quadrature. The uncertainties in the distance moduli include the uncertainty in $\overline{M}_{\text{F160W}}$ of 0.05 mag. Typical values for the individual uncertainties are listed in Table 5. We also determined the range of fluctuation magnitudes permitted given the level of worminess in the background and the agreement between individual annuli. Maximum and minimum values derived from the residual background corrections are listed separately from the other sources of uncertainty in Table 4.

We treated the different uncertainties as if they were independent, but acknowledge the fact that there are subtle correlations between sources of uncertainty that are difficult to quantify. For example, the procedure that is used to fit and subtract the smooth galaxy profile is affected by errors in sky subtraction. While relationships between sources of uncertainty exist, they are insignificant to the results of this study. Examination of Table 5 shows that the significant sources of uncertainty in the distance measurement are the PSF fit, globular cluster correction, and the intrinsic scatter in the $\overline{M}_{\text{F160W}}$ calibration. The first is due mainly to variations in the drift and focus of the telescope and brightness of the PSF stars. The second is principally a function of the depth of the observation and size of the globular cluster population. The cosmic scatter in $\overline{M}_{\text{F160W}}$ is a result of variations in the stellar populations of galaxies. These uncertainties are independent and may safely be added in quadrature. Furthermore, in many cases even these uncertainties are secondary to the larger uncertainty in the correction for worminess in the background, which is a function of time since the last SAA passage.

Measuring the uncertainty due to residual background patterns was difficult; to make an estimate, we explored the range of correction that is permitted by the data by subtracting various levels of uniformly distributed residual spatial power, and thereby found the maximum and minimum fluctuation magnitudes allowed. The most likely fluctuation magnitude for each galaxy was determined taking into account the details described in the notes in the appendix. Rather than assume a Gaussian distribution of errors about the most probable value, we chose to adopt a probability distribution that increases linearly from zero at the maximum and minimum allowed values to the most likely value and is normalized appropriately. The probability function is not symmetrical about the most likely value because the measurement is not usually midway between the maximum and minimum allowed values. We convolved this skewed saw-tooth distribution function with the normal probability distribution of the other sources of uncertainty to get the probability distribution function that was used to determine H_0 .

Some systematic errors listed in Table 5 affect all our measurements equally, and are not included in the uncertainties in Table 4. The first of these is the 0.02 mag uncertainty in the photometric zero point of the F160W filter in the NIC2 camera. The other systematic errors we inherit from the Cepheid distances adopted, either directly or via the I -band SBF calibration. The systematic uncertainty in the Cepheid distance scale of 0.16 mag includes the 0.13 mag uncertainty in the distance to the LMC and the 0.02 mag uncertainty in the zero point of the period-luminosity relationship for Cepheid variables. The systematic photometric uncertainty in the WFPC-2 measurements contributes another 0.09 mag to the Cepheid distances. A detailed discussion of these uncertainties can be found in Ferrarese et al. (2000a). Adding all sources of systematic uncertainty in quadrature gives 0.16 mag. An additional systematic uncertainty from the I -band SBF distance scale is not included because the I -band distances are only used to link the Cepheid calibration to the distant galaxies of our sample. The I -band SBF systematic uncertainties are the same as those already discussed, and it would not be correct to include them twice. The 0.01 mag agreement between the I -band SBF and the direct Cepheid calibrations confirms that no additional systematic

error is incurred by adopting the I -band SBF distances for the calibration.

6.2. Radial Velocities

The heliocentric velocity for each cluster or galaxy was initially measured or collected from the literature by Postman & Lauer (1995, and references therein). The uncertainties on the individual redshift measurements were typically 60 km s^{-1} . New data now available provide velocities to additional cluster members and have been included in this study. Radial velocities are compiled in Table 4, along with the number of individual galaxy redshifts that were averaged to get the cluster velocity. The details of how galaxies were selected for inclusion are described by Postman & Lauer (1995). The mean uncertainty in the mean cluster redshift is 184 km s^{-1} for the Postman & Lauer sample. NGC 4709 is listed in Table 4 with its own radial velocity; it is a member of the high-velocity (4500 km s^{-1}) component of the Centaurus cluster, and hence has a significant peculiar velocity. NGC 5193 is also listed with its own redshift; it was previously thought to be the cD galaxy in Abell 3560, but Willmer et al. (1999) found that it is in fact a foreground galaxy. NGC 4073 is not associated with a cluster; its heliocentric velocity was taken from Beers et al. (1995). The heliocentric velocities were converted to the reference frame that is at rest with respect to the cosmic microwave background (CMB) radiation. The CMB dipole adopted was that measured by Lineweaver et al. (1996).

6.3. The Model Velocity Field and H_0

Measurements of the Hubble constant within 50 Mpc must take peculiar velocities into account because they can be a significant fraction of the Hubble velocity. In fact, one of the differences between the Hubble constants measured by Tonry et al. (SBF-II) and Ferrarese et al. (2000a) using the *same* Cepheid calibrators and the *same* SBF measurements (albeit with a slightly different calibration) was the result of different assumptions about the local velocity field. We have chosen our distant sample to be distributed in such a way as to minimize sensitivity to local peculiar velocities (Fig. 1). By far the greatest immunity to peculiar velocities comes from reaching much greater distances than previously possible. At 130 Mpc, we expect peculiar velocities to be approximately 3% of the Hubble velocity. This insensitivity to peculiar velocities and isotropic distribution of the distant sample produced the most accurate SBF measurement of H_0 to date.

We followed the SBF-II maximum-likelihood procedure for computing H_0 . We first constructed a model velocity field, which included a 187 km s^{-1} cosmic thermal velocity dispersion. The quadrupole term adopted in SBF-II was not included. Various dipole terms (resulting from the peculiar velocity of the Local Group in the CMB frame) were tried, and a comparison is presented below.

At the position of each galaxy as defined by the F160W SBF distance, the most likely velocity

was determined from the velocity model. A number of points were then chosen radially spanning the range of possible distances given the uncertainties in the measured distances. At each point, the joint likelihood of a given combination of distance and velocity measurements was computed, and the likelihood integrated across the radial range in distance. The Hubble constant is a free parameter of the velocity model, and this procedure was repeated to find the value of H_0 which maximizes the likelihood of all the distance and velocity measurements together. This procedure used the distance probability distribution function constructed by convolving the normal Gaussian uncertainties with the saw-tooth probability distribution between the maximum and minimum $\overline{m}_{\text{F160W}}$ values. In practice, we attempted to *minimize* the negative likelihood statistic \mathcal{N} (see SBF-II for details). The value of χ^2 determined using the maximum likelihood technique and our non-Gaussian probability distributions is not necessarily minimized when \mathcal{N} is minimized; however, the difference between values of \mathcal{N} for different input parameters to the velocity model is equivalent to a difference in χ^2 . In Table 6 we compared the likelihood of various models by indicating the difference in χ^2 relative to the baseline model that ignores all peculiar velocities except the motion of the Local Group in the CMB frame.

Several velocity models were used to determine the sensitivity of the H_0 measurement to the input parameters of the models. Results for these tests are listed in Table 6. NGC 4709 was excluded from all fits because the velocity field of the complex Centaurus cluster was not included in the velocity model. The models tried were constructed as follows:

(1) The first model does not include any local attractors or peculiar velocities beyond that of the Local Group in the CMB frame. In the CMB frame, $H_0=76.1 \text{ km s}^{-1} \text{ Mpc}^{-1}$. We adopt the CMB model as the baseline and compare other models by computing the change in χ^2 relative to this case.

(2) Adding the contributions from the Virgo and GA mass concentrations and dipole as prescribed by SBF-II increases H_0 to 77.1. The slight decrease in χ^2 is not significant. The quadrupole term suggested by SBF-II was not included because it is inappropriate for the distances of the galaxies in our sample (including it would increase χ^2 by 25!).

(3–4) For model 3 we used the dipole determined by Willick & Batra (2000). Model 4 includes the dipole measured by Giovanelli et al. (1998) using Tully-Fisher measurements to many clusters out to redshifts of 9000 km s^{-1} . The likelihood of these two dipole models is essentially the same as the best-fitting SBF-II models and the CMB-only baseline model. The Hubble constant implied by these models is approximately $75.5 \text{ km s}^{-1} \text{ Mpc}^{-1}$. The largest difference in H_0 between models 1 to 4, which have essentially the same likelihood, is only $1.6 \text{ km s}^{-1} \text{ Mpc}^{-1}$.

(5) Like model 2, the fifth model used the mass distribution suggested by SBF-II, but allowed the maximum likelihood procedure to determine the most likely dipole velocity in addition to H_0 . Despite having more freedom to fit the data with three additional degrees of freedom, the fit is worse and $\Delta\chi^2$ is larger. The dipole determined is large, but barely larger than the uncertainty. We have sampled the velocity field with only 16 points spanning a range in distance from 50 to 150

Mpc, and the sample was chosen to minimize sensitivity to streaming motions that could bias the measurement of H_0 . Towards this end we were successful; the small variation in H_0 between the various models confirms this conclusion. On the other hand, to reliably measure the bulk motion of the galaxies in the local universe, distances would need to be measured to a much larger sample of galaxies within the redshift interval of interest (7000 to 10,000 km s^{-1} in this study).

(6) The one dipole presented here that fails to fit our data very well is the large dipole velocity of 689 km s^{-1} measured by Lauer & Postman (1994). Using the Lauer & Postman dipole reduces H_0 by approximately 3 $\text{km s}^{-1} \text{Mpc}^{-1}$, but χ^2 is significantly larger. It is, however, closer to the free dipole of model 5 than the other model dipoles considered.

Based on the full data set, we conclude that

$$H_0 = 76 \pm 1.3 \text{ (random)} \pm 6 \text{ (systematic)} \text{ km s}^{-1} \text{ Mpc}^{-1}. \quad (8)$$

The $1\text{-}\sigma$ random uncertainty formally includes all sources of uncertainty in the distance measurement, including the non-Gaussian uncertainty from the residual background correction. Although χ^2 per degree of freedom is not minimized for our non-Gaussian probability distribution, its value of 1.0 for model 1 indicates that the adopted uncertainties are reasonable. The Gaussian $1\text{-}\sigma$ error bars are plotted with thick lines in the Hubble diagram (Fig. 7). The full non-Gaussian ranges allowed by the various corrections to the SBF distances are indicated by the lighter lines underneath each point. The Hubble diagram is shown using the CMB velocities (model 1), and our best-fit value of $H_0=76 \text{ km s}^{-1} \text{ Mpc}^{-1}$ is indicated by the dashed line.

A second line in Figure 7 indicates the decrease in H_0 beyond 70 $\text{h}^{-1} \text{ Mpc}$ ($\sim 7000 \text{ km s}^{-1}$) suggested by Zehavi et al. (1998). Their ‘‘Hubble bubble’’ model hypothesizes that a locally underdense region of the Universe gives rise to an expansion rate about 6% higher within 70 $\text{h}^{-1} \text{ Mpc}$. The SBF analysis was repeated using only the six most distant galaxies and the model 3 (SBF-II) velocity model (model 7 in Table 6). The six galaxies were chosen to minimize H_0 and provide the best match to the decrease in H_0 predicted by Zehavi et al. (1998). The result, 72.3 $\text{km s}^{-1} \text{ Mpc}^{-1}$, reproduces nearly perfectly the predicted decrease in H_0 .

The lower panel in Figure 7 shows the Hubble ratio v_{CMB}/d for each galaxy. The error bars are shown for the Gaussian component of the distance error, and do not include the uncertainty range from the residual background correction. The curved lines behind each point show the full range of possible distances if a different background correction P_g were adopted. The longest arcs are necessarily those points with the worst worminess, the largest corrections, and the lowest S/N ratios. The best-fit value of $H_0 = 76 \text{ km s}^{-1} \text{ Mpc}^{-1}$ is indicated by the horizontal line. Once again, the Zehavi et al. (1998) predicted decrease in H_0 is shown.

We also explored the sensitivity of our results to the low-S/N observations. Several of the measurements are quite poor, and should arguably be excluded from the fits. Excluding all galaxies obviously contaminated by worms (Abell 262, 2666, 3389, 3581, 3742 and NGC 4073) gives $H_0 = 77.4 \pm 1.7 \text{ km s}^{-1} \text{ Mpc}^{-1}$ for model 2, which is nearly the same value determined using the

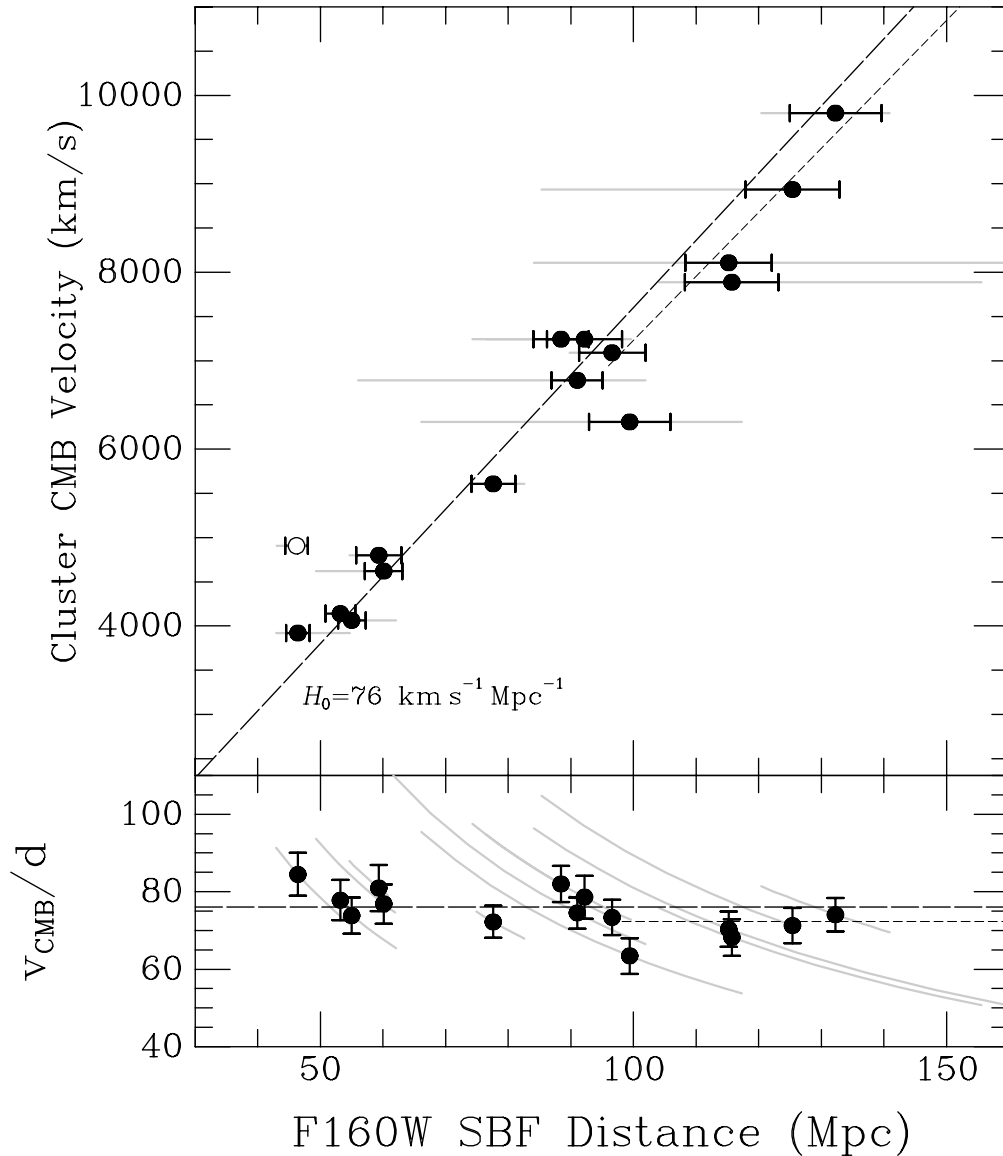


Fig. 7.— The Hubble diagram is plotted for the sample galaxies using their velocities in the CMB frame. The $1\text{-}\sigma$ error bars shown indicate the contributions from the scatter in the F160W SBF calibration, the PSF normalization, sky subtraction, galaxy subtraction, bias subtraction, and globular cluster removal, all added in quadrature. The underlying gray lines indicate the full range of allowed distances as quantified in Table 4 as “max” and “min” values. Our best-fit Hubble constant of $76 \text{ km s}^{-1} \text{ Mpc}^{-1}$ is indicated; NGC 4709 (open symbol) is excluded from the fit. The second dashed line at $H_0 = 72.3 \text{ km s}^{-1} \text{ Mpc}^{-1}$, determined using only the six galaxies more distant than 96 Mpc, shows the 6% reduction in H_0 beyond $70 \text{ h}^{-1} \text{ Mpc}$ suggested by Zehavi et al. (1998). The lower panel shows the Hubble ratio v/d for each point (including a nominal 200 km/s uncertainty in the velocities for illustrative purposes only). The allowed ranges are plotted as dotted curves, indicating how v/d changes with a change in the adopted distance for a particular galaxy. The lower value of H_0 for the outer six points is also shown.

entire data set of 77.1. If we exclude only the three galaxies with $\xi < 1$ (Abell 2666, Abell 3389, and Abell 3581), then we find that $H_0 = 78.0 \pm 1.6$. It is clear that the worst measurements are not systematically biasing the measurement of H_0 . This is not surprising, as the maximum likelihood code takes into account the large range of possible distances for these galaxies. The fact that there is no systematic offset shows that the P_g corrections are applied uniformly and that the residual background is not systematically over or under-subtracted. When the six galaxies that have dust lanes or disks are excluded (Abell 262, 1060, 2199, 3565, 3581, and NGC 5193), $H_0 = 75.7 \pm 1.5 \text{ km s}^{-1} \text{ Mpc}^{-1}$. This value is only $1.4 \text{ km s}^{-1} \text{ Mpc}^{-1}$ smaller than 77.1, and suggests that clumpy dust in some galaxies does not introduce a significant bias to the distance measurements. If there were a significant bias in the distance measurements due to residual cosmic rays, clumpy dust, improper bias removal, undetected globular clusters, or any of the other sources of variance discussed above, the result would be increasingly underestimated distances as redshifts increase. In fact, the opposite trend is observed: the highest redshift galaxies have somewhat larger measured distances than expected, as predicted by the Zehavi et al. (1998) Hubble bubble model.

7. Can H_0 be $65 \text{ km s}^{-1} \text{ Mpc}^{-1}$?

Several groups have recently reported measurements of the Hubble constant derived from HST Cepheid distance calibrations of various secondary distance indicators. Our best-fit measurement of $H_0 = 76 \pm 1.3 \pm 6 \text{ km s}^{-1} \text{ Mpc}^{-1}$ is in good agreement (better than 1σ) with several, including optical SBFs (SBF-II; Lauer et al. 1998), Cepheid distances alone (Willick & Batra 2000), fundamental plane distances (Kelson et al. 2000), and Tully Fisher distances (Sakai et al. 2000). The SBF Hubble constant as calibrated by Ferrarese et al. (2000a) differs from ours at the 1.5σ level for the same reasons it differs from SBF-II: a slightly different SBF calibration and different peculiar velocities were adopted for the four clusters measured by Lauer et al. (see Ferrarese et al. for a discussion). Our measurement of H_0 differs significantly from the results based on type-Ia supernovae. Gibson et al. (2000) report $H_0 = 68 \pm 2 \pm 5 \text{ km s}^{-1} \text{ Mpc}^{-1}$, 12% lower than our value. Parodi et al. (2000) found $H_0 = 58.5 \pm 6.3 \text{ km s}^{-1} \text{ Mpc}^{-1}$ (90% confidence level), which is 24% smaller. These two supernovae measurements cannot be directly compared, however, because of a significant difference (0.18 mag) between the calibration adopted by Parodi et al. and that used by the HST Key Project team (ie., Gibson et al.) The Key Project Cepheid calibration was adopted for this study.

Is it possible that $H_0 = 65 \text{ km s}^{-1} \text{ Mpc}^{-1}$, and that we have overestimated it by 15% (or more)? Roughly one third of this difference disappears if the Zehavi et al. (1998) Hubble bubble model is correct. If galaxies nearer than $\sim 7000 \text{ km s}^{-1}$ must be disregarded because of their enhanced velocities away from a locally under-dense region, then our measurement of H_0 can be as low as $72 \text{ km s}^{-1} \text{ Mpc}^{-1}$. Our results do not demand that this be the case, however, and are still consistent with observations that refute the Hubble bubble hypothesis (Giovanelli et al. 1999, Lahav 2000). The fits including all the data, assuming a smooth Hubble flow, are equally good because the nearer

measurements tend to be most reliable.

Extinction from clumpy dust in the individual galaxies could add to the fluctuation power and bias the SBF measurements to shorter distances. No sign of dust was seen in the images of the galaxies used to determine the calibration of $\overline{M}_{\text{F160W}}$ (aside from NGC 1387 and NGC 4536, which were excluded). Six of the distant galaxies do have obvious dust lanes (Table 2). Only one (Abell 262) has extensive dust, and we used the optical WFPC-2 image of Lauer et al. (1998) to mask the dusty regions. The other five have dust lanes or disks that are concentrated near the centers of the galaxies, which were masked. There is no evidence for extended patches of dust with sizes comparable to the PSF and smooth on larger scales. The distances for these are not systematically smaller than the others at the same redshifts, nor are their colors redder on average. The Hubble constant measured with the six dusty galaxies excluded was not significantly smaller, and it seems unlikely that all the distant galaxies would have uniformly distributed clumpy dust that would be unrecognizable in our images.

Besides the potential 6% reduction in H_0 beyond ~ 100 Mpc suggested by the six most distant measurements, are there systematic problems with the F160W SBF measurements that could explain another $\sim 10\%$ (or more) difference between our results and the conclusions of the supernovae measurements? There are potentially three sources of extra power in the power spectrum that are not convolved with the diffraction pattern of the telescope, but do have power on the spatial scales over which we fit the SBF power spectrum. The first of these is the residual bias scaled by the flat field image. We addressed this possibility by explicitly subtracting a dithered bias \times flat image as described in Section 3. The uncertainty in H_0 resulting from errors in bias subtraction was measured and found to be less than 1% (Table 5).

The second potential contributor to the power spectrum is the residual wormy background. We carefully excluded wormy images and subtracted an estimate of the residual power as described in Section 3. If the correction for worms were systematically underestimated, then our measurement of H_0 would be too large. In the previous section we showed that excluding the galaxies contaminated by worms had no significant effect on the measurement of H_0 . Excluding the lowest S/N measurements also had no significant effect. The range of H_0 values seen during these tests was less than $1 \text{ km s}^{-1} \text{ Mpc}^{-1}$. This suggests that the corrections were applied uniformly.

The third potential contributor to the power spectrum is the residual structure in the background from subtraction of the model galaxy profile. To avoid any bias because of the somewhat arbitrary fit of the left-over large-scale structure in the galaxy, we excluded wavenumbers smaller than 20 from our analysis. The mean uncertainty in the distance modulus from galaxy and smooth background subtraction was 0.02 mag. Residual galactic structure could explain a 1% bias in our H_0 measurement, but not a large systematic error.

If the fluctuation powers we measure are reliable, is it possible that other sources of systematic error could cause us to overestimate H_0 by 10 to 15%? Perhaps the most obvious candidate for this kind of systematic error would be the calibration of the F160W absolute fluctuation magnitude. We

used both Cepheid and I -band SBF distances to determine the calibration. Although not completely independent, the two calibrations are remarkably consistent (0.01 mag). The agreement between the I -band SBF and direct Cepheid calibration supports the conclusion that there is no significant difference in the fluctuation amplitudes between early and late-type galaxies. The applicability of the calibration to the more distant galaxies is demonstrated by the overlap with the intermediate-distance sample. To explain a 15% difference in H_0 , $\overline{M}_{\text{F160W}}$ would have to be brighter by 0.3 mag, or $\overline{M}_{\text{F160W}} = -5.16$. Examination of Figure 5 shows that a calibration as bright as -5.16 is inconsistent with the data.

Significant systematic errors in the Cepheid distance scale are relevant to the measurement of the true value of the Hubble constant, but cannot explain the difference between our measurement and that determined using type-Ia supernovae because we adopted the same Cepheid calibration as the other groups listed at the beginning of this section. A systematic error in the distance to the LMC (for example) will affect our measurement of H_0 in exactly the same way as the other measurements.

Is it possible that the mundane choice of Galactic extinction corrections could result in a systematic calibration error at the 15% level? By observing in the near-IR, our sensitivity to errors in the extinction are significantly reduced. The largest correction in our sample is 0.08 mag (Table 1). Most of the calibrator galaxies have IR extinction corrections of order 0.01 mag. If extinction has been underestimated, the true fluctuation magnitudes will be brighter than we have estimated and the distances smaller. Increasing extinction corrections makes H_0 larger. On the other hand, extinction cannot have been overestimated by very much because the corrections are already very close to zero. The only other way to get distance measurements that are systematically underestimated by 15% would be for extinction corrections to all three Cepheid calibrators used in this paper and all the Cepheid calibrators used by Tonry et al. (SBF-II) to be overestimated by 0.3 mag, but not those used to calibrate the supernova distance scale. It seems unlikely that Galactic extinction could be the cause of so large a systematic error.

One reason that previous measurements of H_0 have disagreed with each other has been the choice of velocities used (Ferrarese et al. 2000a, Mould et al. 2000). When H_0 is measured on scales where the peculiar motions of individual galaxies are a significant fraction of the Hubble velocity, the value of H_0 will depend quite sensitively on the velocity adjustments made for infall into local mass concentrations. Our measurement of H_0 reaches well into the Hubble flow and is distributed uniformly on the sky, and is therefore very insensitive to the choice of velocity model and the peculiar velocities of individual galaxies and clusters (as described in Section 6.3).

Finally, we cannot rule out the possibility that modest systematic errors affect both F160W SBF and type-Ia supernovae distance measurement techniques in such a way to create the difference between the measurements.

8. Summary

We measured accurate IR SBF distances to a collection of 16 uniformly-distributed distant galaxies for the purpose of measuring the Hubble constant well beyond the influence of local peculiar velocities. These NICMOS measurements mark the first time SBFs have been measured in galaxies out to redshifts of $10,000 \text{ km s}^{-1}$, clearly demonstrating the advantages of measuring SBFs in the near-IR with excellent spatial resolution and low background. The calibration of the F160W SBF distance scale presented here was based on SBF measurements of galaxies in which Cepheid variable stars were detected in the same galaxy. Using a maximum-likelihood technique to account both for the influence of local mass concentrations on the velocity field and the non-Gaussian uncertainties on our SBF distance measurements yields a Hubble constant of $H_0 = 76 \pm 1.3 \text{ km s}^{-1} \text{ Mpc}^{-1}$ ($1\text{-}\sigma$ statistical uncertainty) with an additional systematic uncertainty of $6 \text{ km s}^{-1} \text{ Mpc}^{-1}$, primarily the result of uncertainty in the distance to the LMC. The small statistical uncertainty in H_0 is a result of the fact that our measurement is very insensitive to peculiar velocities, stellar population variations, extinction corrections, and photometric errors. Arbitrarily excluding all but the six most distant galaxies from the fit results in a 6% decrease in H_0 , consistent with the hypothesis that the Local Group is located in an under-dense region of the universe.

This study benefitted greatly from NICMOS data collected as part of several programs, and we thank those who worked to acquire that data. In particular, we are grateful to those who helped ensure that the data would be appropriate for SBF analysis and assisted with the data reductions (D. Geisler, J. Elias, J. R. Graham, and S. Charlot). We are indebted to the NICMOS GTO team for their hard work in building, calibrating, and providing software for NICMOS. We greatly appreciated the helpful comments of R. Weymann, J. Blakeslee, and L. Ferrarese. The calibration presented here made use of data collected by the Optical SBF team (J. Tonry, J. Blakeslee, E. Ajhar, and A. Dressler), and we thank them for providing color photometry and *I*-band SBF distances to the calibration galaxies. Finally, we wish to thank G. Worthey, S. Charlot, and A. Vazdekis for constructing stellar population models and providing appropriate $k(z)$ -corrections.

This research was supported in part by NASA grant GO-07453.0196A. The NICMOS GTO team was supported by NASA grant NAG 5-3042. J. Jensen acknowledges the support of the Gemini Observatory, which is operated by the Association for Research in Astronomy, Inc., under a cooperative agreement with the National Science Foundation on behalf of the Gemini partnership: the National Science Foundation (United States), the Particle Physics and Astronomy Research Council (United Kingdom), the National Research Council (Canada), CONICYT (Chile), the Australian Research Council (Australia), CNPq (Brazil) and CONICET (Argentina).

A. Appendix: Notes

Abell 262 (NGC 708): The central galaxy in Abell 262 is littered with dust. We used the high-resolution *I*-band WFPC-2 images (Lauer et al. 1998) to identify dusty regions and create a mask for our NICMOS image. In addition to the copious dust, we had to exclude exposures because of worminess in the background. The uncertainty in fluctuation magnitude is relatively large because of the dustiness and wormy background corrections, even though Abell 262 is among the closest of the clusters we observed.

Abell 496 (PGC 015524): This cluster is the most distant in our sample, and we allocated 3 orbits to ensure a good SBF measurement. Of the 20 individual exposures, only the last two were found to be wormy. The other 18 are unaffected. The S/N is good and the fluctuation measurement is reliable.

Abell 779 (NGC 2832): Aside from a little dither-pattern noise in the power spectrum, the results for Abell 779 are quite good. Pattern noise is an array of spots in the spatial power spectrum with a periodicity corresponding to the 20-pixel offset of the dither pattern. Detector artifacts (e.g., vertical bands or mismatches in the background level at quadrant boundaries) were sometimes incompletely removed by the image reduction procedures and cause pattern noise. Pattern noise is only significant in the power spectrum of the outermost annulus.

Abell 1060 (NGC 3311): The central galaxy in the Hydra cluster was one of four galaxies presented here that were observed by D. Geisler, J. Elias and E. Ajhar as part of NICMOS program 7820. The images were reduced for SBF analysis using the software and procedures described in this paper. NGC 3311 has some dust in the central region that was masked; the SBF fit in the outer regions is nearly perfect and the S/N ratio is very high.

Abell 1656(a) (IC 4051): Two galaxies in the Coma cluster were observed by D. Geisler et al. IC 4051 has an unusually large population of globular clusters (Baum et al. 1997). We found that many are much brighter than expected for a galaxy at this distance. We modified the luminosity fitting parameters and estimated the contribution from unresolved GCs and subtracted it, but a relatively large uncertainty in the GC contribution to the SBF power remains. The fit to the SBF power spectrum is good.

Abell 1656(b) (NGC 4874): The power spectrum for NGC 4874 is clean and the fit is very good. NGC 4874 has a normal globular cluster population (Harris et al. 2000).

Abell 2199 (NGC 6166): The central galaxy in Abell 2199 has dust lanes within 3 arcsec of the center. The dust lanes were masked prior to performing the SBF analysis, but measurements in the innermost aperture are suspect. The SBF analysis did not include the region between NGC 6166 and two nearby companions, where the fit to the galaxy profile is not very good. The fit to the power spectrum in the intermediate annulus was excellent, but the outer two apertures disagree at a level (0.64 mag) that cannot be corrected properly by adopting a value of P_g that scales with area. We adopted the measurement in the intermediate aperture and a relatively large range of

permitted fluctuation magnitudes.

Abell 2666 (NGC 7768): NGC 7768 has surprisingly few globular clusters, which is consistent with the measurements of Harris, Pritchett, & McClure (1995) and Blakeslee, Tonry, & Metzger (1997). Our attempts to fit a luminosity function to a half-dozen objects failed to produce a reasonable correction for undetected globular clusters. The SBF analysis proceeded without a GC correction, and we adopted an uncertainty that is larger than the other galaxies that reflects our lack of knowledge of the GC luminosity function. The only way this measurement could be significantly biased by undetected GCs is if the GC luminosity function is skewed to the faint end and contains practically no GCs on the bright side of the peak. The Abell 2666 observation is also contaminated by a wormy background. One of the six exposures is excluded, and the worst regions masked in the two subsequent exposures. There is always a tradeoff between including frames that increase the SBF signal but also contain the decaying wormy background. In this case, a good fit to the power spectrum was achieved, but a significant correction for the background must be applied to make the outer two apertures agree. P_g is further enhanced by the presence of undetected globular clusters and background galaxies that could not be handled with the usual procedure of fitting luminosity functions due to the paucity of bright objects in this field. $\xi < 1$ for this galaxy and the possible range of fluctuation magnitudes is therefore quite large.

Abell 3389 (NGC 2235): We observed the central galaxy in Abell 3389 in the continuous viewing zone to achieve a longer total integration time for this galaxy. Unfortunately, the longer MULTIACCUM sequences used to avoid frequent NICMOS buffer dumps had many more persistent cosmic rays in each image and a significantly wormy background. We abandoned half of our images, and the remaining ones must be corrected for residual worminess. As a result, P_g is significant and ξ is less than unity. The fluctuation power increases significantly with aperture area, and the globular cluster and worminess corrections are large. The uncertainties reflect the fact that the fluctuation magnitude is poorly constrained.

Abell 3565 (IC 4296): IC 4296 has a compact dust ring close to the nucleus, but no sign of dust outside of a radius of 1.5 arcsec. Very small residual spatial variance corrections (P_g) bring the annuli into nearly perfect agreement. The S/N of this measurement is high and the GC correction small.

Abell 3581 (IC 4374): the observations of IC 4374 were strongly affected by worminess in the background. Two of six exposures were excluded from the final image, and residual worms were masked in three of the remaining four. The potential for bias is strong in this case, and a significant P_g correction for background power was applied, resulting in a $\xi < 1$ and a large range of allowed fluctuation magnitudes. Furthermore, the central regions contain a dust lane, which we masked.

Abell 3656 (IC 4931): The only problem that arose in the analysis of IC 4931 is the presence of dither pattern noise in the background. This problem is only significant in the largest annulus; the inner two agree nicely.

Abell 3742 (NGC 7014): The HST failed to lock onto the guide stars for the observations of

NGC 7014. Because some drift occurred during the MULTIACCUM sequences, our IDL procedures interpreted the changing flux in each pixel as cosmic rays. To overcome this problem, we were forced to abandon the temporal cosmic ray rejection and rely on the spatial information alone. The galaxy fitting routine also had trouble because of the smeared image. The residual image shows extra background structure close to the center where the galaxy fit is worst. In this case, we included a small correction to the fluctuation power that scales as the galaxy brightness (rather than by the area of the aperture, as with the worminess corrections applied to some of the other galaxies). Furthermore, the S/N is reduced because the PSF has been smeared by telescope drift. Because the bright PSF stars used for the other galaxies do not match in this case, we resorted to extracting a low-S/N PSF from a combination of six faint stars or globular clusters from the smeared image of NGC 7014. The resulting fit is acceptable, but the PSF normalization somewhat uncertain. Although Abell 3742 is among the closest clusters in our sample, the uncertainties are relatively large.

NGC 4073: This galaxy was observed by D. Geisler et al., and it is not associated with a cluster. Its globular cluster population is extensive. Worminess in some of the images contaminates the SBF measurement, and the P_g correction is large. Another difficulty with the analysis of this galaxy was accurately subtracting the smooth galaxy profile. Because of the dither pattern used in this case was chosen to maximize the number of globular clusters detected, there is a hole in the image near the galaxy center that made galaxy subtraction somewhat difficult.

NGC 4709: This galaxy is part of the complex Centaurus cluster and has a significant positive peculiar radial velocity. Although it is not useful for measuring the Hubble Constant, it does have a reliable *I*-band SBF distance from WFPC-2 observations. The first of the six exposures was excluded because of low-level worminess in the background. The resulting power spectrum fits the PSF spectrum very well, and the S/N is relatively high. A modest correction for background worminess brought the individual apertures into perfect agreement

NGC 5193: A recent velocity study by Willmer et al. (1999) indicated that NGC 5193 is not a member of the Abell 3560 cluster, as had been supposed. NGC 5193 has a dust ring extending 2.6 arcsec from the center, which we masked. NGC 5193 is one of the nearest galaxies in our survey, and the S/N ratio is quite high. Nevertheless, the relatively large range of acceptable fluctuation magnitudes reflects the 0.5 mag disagreement between annuli that was not removed with a uniform P_g correction.

Table 5. Typical Uncertainties

Source	σ
<i>Random Uncertainties</i>	
PSF normalization and fitting	0.06 mag
Sky subtraction	0.01 mag
Globular cluster and background galaxy removal	0.07 mag
Galaxy profile subtraction	0.02 mag
Bias subtraction	0.01 mag
Wormy background correction (see text)	~ 0.08 mag
\overline{M}_{F160W} calibration	0.05 mag
CMB Velocities	200 km s^{-1}
<i>Systematic Uncertainties</i>	
NICMOS photometric zero point	0.02 mag
Cepheid distance calibration	0.16 mag

Table 6. Values of H_0 for Different Velocity Models

Model	Fixed Model Components ^a	Dipole (l, b)	Dipole v (km s ⁻¹)	H_0 (km s ⁻¹ Mpc ⁻¹)	$\Delta\chi^2$ ^b	Reference
(1)	CMB only.....	76.1±1.3	0.0	Lineweaver et al. 1996
(2)	Virgo, GA & dipole....	(306,43)	205±83	77.1±1.6	-0.2	SBF-II
(3)	Willick & Batra dipole .	(274,67)	243	75.6±1.3	0.2	Willick & Batra 2000
(4)	Giovanelli et al. dipole .	(295,28)	151±120	75.5±1.3	0.4	Giovanelli et al. 1998
(5)	Virgo, GA & dipole ^c	(355,56)	409±335	76.9±1.5	1.4	SBF-II+free dipole
(6)	Lauer & Postman dipole	(343,52)	689±178	73.8±1.5	9.7	Lauer & Postman 1994
(7)	Model (2) + Bubble ^d ...	(306,43)	205±83	72.3±2.3	...	Zehavi et al. 1998

^aAll models include a cosmic velocity dispersion of 187 km s⁻¹ as in SBF-II.

^bThe relative likelihood of each model is quantified here as a difference in units of χ^2 from the baseline CMB model (1).

^cThe dipole term is a free parameter in this model, and $\Delta\chi^2$ has been adjusted to account for the three additional degrees of freedom. The positions of the Virgo and Great Attractor clusters are fixed as in SBF-II, without the quadrupole term.

^dModel components are the same as in (2), but only the six galaxies more distant than 96 Mpc outside the putative locally under-dense region are used to compute H_0 .

REFERENCES

- Ajhar, E. A., Lauer, T. R., Tonry, J. L., Blakeslee, J. P., Dressler, A., Holtzman, J. A., & Postman, M. 1997, *AJ*, 114, 626
- Baum, W. A., Hammergren, M., Thomsen, B., Groth, E. J., Faber, S. M., Grillmair, C. J., & Ajhar, E. A. 1997, *AJ*, 113, 1483
- Beers, T. C., Kriessler, J. R., Bird, C. M., & Huchra, J. P. 1995, *AJ*, 109, 874
- Blakeslee, J. P., Ajhar, E. A., & Tonry, J. L. 1999, in *Post-Hipparcos Cosmic Candles*, eds. A. Heck & F. Caputo (Boston: Kluwer Academic Publishers), 181
- Blakeslee, J. P. & Tonry, J. L. 1995, *ApJ*, 442, 579
- Blakeslee, J. P., Tonry, J. L., & Metzger, M. R. 1997, *AJ*, 114, 482
- Blakeslee, J. P., Vazdekis, A., & Ajhar, E. A. 2000, *MNRAS*, in press
- Baum, W. A., Hammergren, M., Thomsen, B., Groth, E. J., Faber, S. M., Grillmair, C. J., & Ajhar, E. A. 1997, *AJ*, 113, 1483
- Ferrarese, L. et al. 1998, *ApJ*, 507, 655
- Ferrarese, L. et al. 2000a, *ApJ*, 529, 745
- Ferrarese, L. et al. 2000b, *ApJS*, in press
- Ferrarese, L., Silbermann, N. A., Mould, J. R., Stetson, P. B., Saha, A., Freedman, W. L., & Kennicutt, R. C., Jr. 2000c, *PASP*, 112, 117
- Freedman, W. et al. 1994, *ApJ*, 427, 628
- Gibson, B. K. et al. 1999, *ApJ*, 512, 48
- Gibson, B. K. et al. 2000, *ApJ*, 529, 723
- Giovanelli, R., Dale, D. A., & Haynes, M. P. 1999, *ApJ*, 525, 25
- Giovanelli, R., Haynes, M. P., Salzer, J. J., Wegner, G., da Costa, L. N., & Freudling, W. 1998, *AJ*, 116, 2632
- Graham, J. A. et al. 1997, *ApJ*, 477, 535
- Harris, W. E., Kavelaars, J. J., Hanes, D. A., Hesser, J. E., & Pritchett, C. J. 2000, *ApJ*, 533, 137
- Harris, W. E., Pritchett, C. J., & McClure, R. D. 1995, *ApJ*, 441, 120
- Jensen, J. B., Tonry, J. L., & Luppino, G. A. 1998, *ApJ*, 505, 111

- Jensen, J. B., Tonry, J. L., & Luppino, G. A. 1999, *ApJ*, 510, 71
- Jensen, J. B., Tonry, J. L., Barris, B. J., Thompson, R. I., Liu, M. C., Ajhar, E. A., Lauer, T. R., Rieke, M., & Postman, M. 2000, in preparation
- Kavelaars, J. J., Harris, W. E., Hanes, D. A., Hesser, J. E., & Pritchett, C. J. 2000, *ApJ*, 533, 125
- Kelson, D. et al. 2000, *ApJ*, 529, 768
- Kennicutt, R. C., Jr. et al. 1998, *ApJ*, 498, 181
- Lahav, O. 2000, in *Cosmic Flows 1999: Towards an Understanding of Large-Scale Structure*, eds. S. Courteau, M. A. Strauss & J. A. Willick (Chelsea: Sheridan Books), 377
- Lauer, T. R. & Postman, M. 1994, *ApJ*, 425, 418
- Lauer, T. R., Tonry, J. L., Postman, M., Ajhar, E. A., & Holtzman, J. A. 1998, *ApJ*, 499, 577
- Lineweaver, C. H., Tenorio, L., Smoot, G. F., Keegstra, P., Banday, A. J., & Lubin, P. 1996, *ApJ*, 470, 38
- Liu, M. C., Charlot, S., & Graham, J. R. 2000, *ApJ*, in press
- Mochejska, B. J., Macri, L. M., Sasselov, D. D., & Stanek, K. Z. 2000, *AJ*, 120, 810
- Mould, J. R. et al. 2000, *ApJ*, 529, 786
- Pahre, M. A. et al. 1999, *ApJ*, 515, 79
- Parodi, B. R., Saha, A., Sandage, G. A., & Tammann, G. A. 2000, *ApJ*, 540, 634
- Postman, M. & Lauer, T. R. 1995, *ApJ*, 440, 28
- Saha, A., Sandage, A., Labhardt, L., Tammann, G. A., Macchetto, F. D., & Panagia, N. 1996, *ApJ*, 466, 55
- Sakai, S. et al. 2000, *ApJ*, 529, 698
- Schlegel D. J., Finkbeiner, D. P., & Davis, M. 1998, *ApJ*, 500, 525 (SFD)
- Stanek, K. Z. & Udalski, A. 1999, submitted (astro-ph/9909346)
- Stephens, A. W., Frogel, J. A., Ortolani, S., Davies, R., Jablonka, P., Renzini, A., & Rich, R. M. 2000, *AJ*, 119, 419
- Thomson, B., Baum, W. A., Hammergren, M., & Worthey, G. 1997, *ApJ*, 483, L37
- Tonry, J. L., Blakeslee, J. P., Ajhar, E. A., & Dressler, A. 1997, *ApJ*, 475, 399
- Tonry, J. L., Blakeslee, J. P., Ajhar, E. A., & Dressler, A. 2000, *ApJ*, 530, 625 (SBF-II)

Willick, J. A. & Batra, P. 2000, ApJ, submitted

Willmer, C. N. A., Maia, M. A. G., Mendes, S. O., Alonso, M. V., Rios, L. A., Chaves, O. L., & de Mello, D. F. 1999, AJ, 118, 1131

Worthey, G. 1994, ApJS, 95, 107

Zehavi, I., Riess, A. G., Kirshner, R. P., & Dekel, A. 1998, ApJ, 503, 483